Coordination Chemistry Reviews 473 (2022) 214840

Contents lists available at ScienceDirect

Coordination Chemistry Reviews

journal homepage: www.elsevier.com/locate/ccr

Review

Molecular clusters in confined spaces

Alan Braschinsky, Jonathan W. Steed *

Department of Chemistry, Durham University, South Road, Durham DH1 3LE, UK

ARTICLE INFO

Article history:
Received 12 July 2022
Accepted 9 September 2022
Available online 24 September 2022

Keywords:
Metal-Organic Frameworks
Nanocages
Confinement Chemistry
Molecular Clusters
Nucleation and Crystallization Under Confinement

ABSTRACT

Confinement chemistry is a growing field with many potential applications in the synthetic, catalytic and especially pharmaceutical industries. Confinement of materials can reveal novel properties as compared to their bulk. They can also give insight into the nucleation and crystallization processes at the nanoscale. In this review, we focus on enclosed molecular clusters, from small aggregates to nucleation effects and ultimately crystallization within confining matrices such as metal–organic frameworks (MOFs), discrete cages, nanopores and droplets ranging from 5 Å to 2 mm. This review aims to impact on the discovery of new drug solid forms, drug delivery, crystal engineering, water harvesting, and gas capture among other topics.

Contents

1. Introduction . . . 1
2. Nanoconfinement in Metal-Organic frameworks . . . 2
   2.1. Inorganic clusters . . . 2
   2.2. Organic clusters . . . 5
   2.3. Solid-state clusters of gases . . . 7
3. Nanoconfinement in cages . . . 10
   3.1. Inorganic clusters . . . 10
   3.2. Organic clusters and solid-state clusters of gases . . . 14
4. Crystallization under confinement . . . 16
   4.1. Crystallization in nanopores . . . 17
   4.2. Crystallization in droplets . . . 19
5. Conclusions . . . 20
   Declaration of Competing Interest . . . 21
   Acknowledgement . . . 21
   References . . . 21

1. Introduction

Confinement plays a key role in many biological processes, and possibly even in the beginnings of life.[1] It can alter chemical reactivities in many ways, particularly in terms of kinetics and selectivity while confinement effects are also involved in the control of various aspects of chemical and biological processes.[2] In the context of the origin of life, for example, it has been suggested that nanoconfinement between layers of mica sheets could have acted to isolate and protect the first protocells.[3] These protocells could be regarded as microreactors that provided compartmentalisation

* Corresponding author.
E-mail address: jon.steed@durham.ac.uk (J.W. Steed).

https://doi.org/10.1016/j.ccr.2022.214840
0010-8545/

for the evolution of living cells.[4] Confinement and compartmentalisation remain essential for the persistence of life on Earth. Eukaryotic life forms involve confinement from the organs down to the subcellular levels. For instance, DNA which is usually pictured as a straight double helix is actually tightly folded and packed into chromatin by proteins called histones.[5] Consequently, compartmentalisation allows biochemical reactions that are consistently performed at amazingly high rates, selectivities, and efficiencies.[6,7].

As a result of this biological inspiration, the study of chemistry and chemical substances under confinement has become a topic of considerable research in recent years. However, confinement chemistry is not a new field. A review article by Gil and Ozin published in 1989 discussed the applications of a variety of guests (organic, metal clusters and coordination compounds) confined in zeolitic hosts.[8] These applications include catalysis, electron transport and gas separation. In 1998, Sheldon *et al.* discussed advances made in the use of confined metal ions in solid-state zeolites as catalysts for liquid phase processes.[9] Crucially, these review articles examined the methods to produce materials which contain confined molecules inside their pores, and subsequently the application of these guest-in-host materials in catalysis.

However, a 2002 article by Levinger discussed confinement chemistry from a wholly different perspective.[10] Levinger pointed out that water under confinement can behave differently compared to its bulk. Confinement of water molecules inside a reverse micelle leads to changes in the vibrational modes in the far-IR region (3–33 cm^{-1}) of reverse micellar water solutions which can dramatically affect various chemical and biological processes.[11] The absorption features in the far-IR region are only observed in micelles with radii between 15 and 45 Å while the spectra of larger aqueous reverse micelles do not show these absorption peaks, which is consistent with bulk water. As a result, the focus of confinement chemistry shifted to studying confinement effects on various molecules and molecular processes including physicochemical properties, ionic and molecular transport and self-assembly.[12–14] In 2005, a landmark review article by McKenna and Alcoutlabi discussed crystallization under confinement.[15] Importantly, the authors concluded that amorphous solids under confinement can exhibit a decreased glass transition temperature. These results suggest that confinement effects could also affect nucleation and subsequently crystal growth processes. Roughly a decade later, Ward and Jiang reviewed advances in this field.[16] An influential discovery within the decade was the recognition by Ward and co-workers of the phenomenon of size-dependent polymorphism, which can have considerable effects on the production of nanosized active pharmaceutical ingredients.[17] This result highlights the growing importance of confinement chemistry which can be increasingly understood due to advances in techniques such as single crystal X-ray diffraction (SXRD) and micro electron diffraction (microED), which allow the study of confinement at ever smaller scales with increasing resolution. Among these results, we aim to highlight other influential reports, many of which are highlighted in Fig. 1, showing the progression of the field of confinement chemistry since 2000.

Recent review articles about the effect of molecular confinement on chemical reactivity (including kinetics, selectivity, and types of reactions), water purification, cancer theranostics, and supramolecular organization highlight further advances in the field.[28–31] As a result, a substantial collection of studies has accumulated on the topic. This review will focus on recent discoveries in confining molecular clusters in extended framework and discrete cage-type materials. In the context of this review, we define confinement as a state in which nanoscale matrices (materials which contain nanosized pores or voids) impose a size restriction on the growth of a particular material or substance and hence herein, confinement is discussed strictly on the nanoscale. Section 2 will discuss nanoconfinement in metal–organic frameworks (MOFs). In particular we highlight the immensely important advance of using MOF single crystals (first introduced and termed the "crystalline sponge" method in 2013 by Fujita and co-workers) to order guest molecules in a crystalline array to allow molecular structure determination.[32] Here we highlight recent review articles published regarding confinement in MOFs.[33,34] These reviews focus on applications of MOF confinement in catalysis and mass transport inside MOF pores. Section 3 will discuss nanoconfinement imposed by discrete cage-type molecules. A recent review published by Fujita and Takezawa discusses confinement effects in self-assembled coordination cages, but their work mainly examines the coordination cages synthesised by their group. Finally, section 5 will discuss crystallization under confinement in nanopores and droplets. In 2020, Jones and Bimbo reviewed the use of mesoporous silicon (pSi) for the control the polymorphism, drug loading and physicochemical properties of active pharmaceutical ingredients and thus we will not discuss pSi in our work. Additionally, He and co-workers recently reviewed chemical synthesis under confinement in porous materials.[35].

2. Nanoconfinement in Metal-Organic frameworks

2.1. Inorganic clusters

The thermal, magnetic and electronic properties of metal nanoparticles (NPs) change with their size. For example, indium NPs with particle size of 10 nm exhibit a 120 °C decrease in the melting point compared to larger clusters of 100 nm.[36] Silver NPs emit green, yellow and red/orange light corresponding to 70,

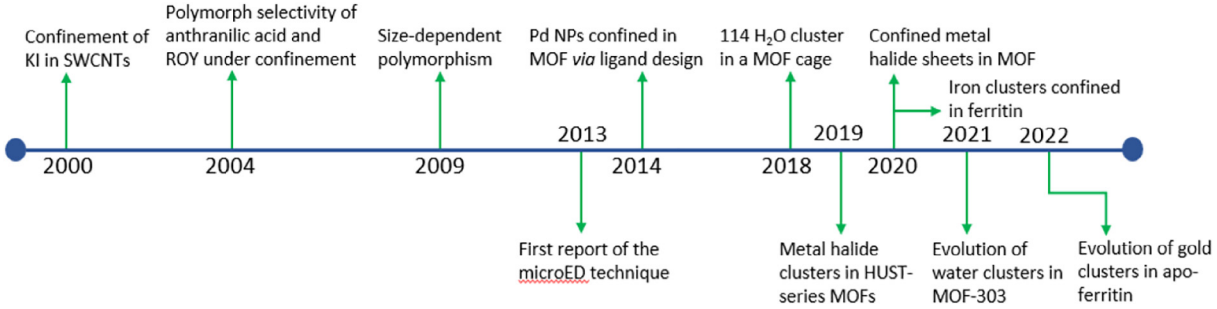

Fig. 1. The development of confinement chemistry since 2000. Important findings from left to right: Confinement of KI in single-walled carbon nanotubes [18], polymorph selectivity of anthranilic acid and 5-methyl-2-[(2-nitrophenyl)amino]-3-thiophenecarbonitrile (ROY) [19], size-dependent polymorphism [17], first solved crystal structure using microcrystal electron diffraction [20], first report of MOF ligand design for NP confinement [21], water molecule cluster of 114 molecules in Cr-soc-MOF [22], metal halide clusters in HUST-series MOFs [23], confined metal halide sheets in $Zr_6O_4(OH)_4(bpydc)_6$ MOF [24], iron clusters confined in ferritin [25], crystallographically observed evolution of water clusters in MOF-303 [26] and evolution of gold clusters inside an apo-ferritin [27].

115 and 140 nm particle sizes, respectively. Being able to control the aggregate size of NPs can thus be beneficial to various electronic and optical applications. This can be achieved by using framework-type materials with well-defined pore sizes as matrices for the synthesis of NPs. In general, two methods to synthesise NPs inside porous coordination networks are used. The first method involves the conversion of encapsulated metal precursors to NPs within the framework pores. The second method is one-pot synthesis of frameworks in the presence of NPs.

A more unique approach to encapsulated nanoparticles was reported by Chen and co-workers in 2014, and involves ligand design to prepare palladium-incorporated UiO-67 MOF (Pd^0-in-UiO-67).[21] In the first step, the authors coordinated palladium (II) chloride to 2,2′-bipyridine-5,5′-dicarboxylic acid (bpydc) to synthesize the metalloligand **1**. Mixing **1** with biphenyldicarboxylic acid and zirconium(IV) chloride ($ZrCl_4$) in DMF gives Pd^{II}-in-UiO-67 *via* a solvothermal method. Subsequent treatment of the framework with hydrogen gas at 250 °C yields encapsulated palladium metallic NPs; Pd^0-in-UiO-67. TEM imaging reveals an average palladium NP size of 3.0 ± 0.5 nm inside the pores of Pd^0-UiO-67. The encapsulated palladium NPs have been used as catalysts for the oxidation of alcohols and reduction of nitrobenzene. The catalytic efficiency of Pd^0-in-UiO-67 for nitrobenzene reduction is comparable to that of the most active palladium catalyst reported.[21].

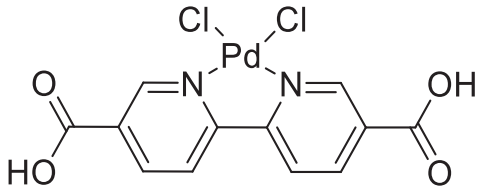

1

A similar approach was taken to synthesise ultrasmall Cu/ZnO_x NPs within another UiO-series MOF UiO-bpy.[37] The solvothermal synthesis of a DMF solution containing $ZrCl_4$, bpydc and formic acid yields UiO-bpy as a white powder. Postsynthetic modification was used to coordinate copper ions to the bipyridine moieties of the framework by simply adding UiO-bpy to a solution containing $CuCl_2$ until the MOF turns green (UiO-bpy-Cu). Additionally, zinc ions can be attached to the zirconium oxide secondary building units by adding $ZnEt_2$ to a solution of UiO-bpy-Cu until the green MOF turns black to form Zn@UiO-bpy-Cu. The MOF can then be reduced at 250 °C and 4 MPa under hydrogen atmosphere to form ultrasmall Cu/ZnO_x NPs inside the UiO-bpy pores (CuZn@UiO-bpy). The resulting material has been characterised by diffuse reflectance UV–vis–NIR spectroscopy and scanning transmission electron microscopy-high angle annular dark-field images. The ZnCu@Uio-bpy material exhibits higher space–time yield and selectivity toward CO_2 hydrogenation to methanol than the commercial ternary $Cu/ZnO/Al_2O_3$. Remarkably, the MOF catalyst exhibits 100 % selectivity for methanol under 200–250 °C.

In previous examples, secondary building units and organic linkers were used to prepare NPs in MOFs. Additionally, the overall charge, in the case of ionic MOFs, can be used to encapsulate and stabilise metal NPs. For instance, ultrasmall metal clusters can also be prepared inside a negatively charged MOF, in which both the confinement effect and charge act to stabilise the metal clusters. This was achieved by Pardo and co-workers who synthesised an anionic MOF $Ni^{II}_2\{Ni^{II}_4[Cu^{II}_2(Me_3mpba)_2]_3\}\cdot 54H_2O$ (**2**) (Fig. 2a) by a transmetallation process of a magnesium-based MOF.[38] Material **2** was then reacted with $[Pd^{II}(NH_3)_4]^{2+}$ and subsequently reduced using $NaBH_4$ to yield compound **3** (Fig. 2b), which contains $[Pd_4]^{2+}$ clusters inside the pores of the anionic MOF. SXRD analysis of **3** shows that the tetranuclear palladium clusters are one- and two-coordinated. Furthermore, the inner Pd–Pd bond lengths (2.57 and 2.44 Å) are considerably shorter than the outer Pd–Pd bond lengths (3.16 and 2.91 Å). This drastic difference in bond lengths within a cluster had not been previously observed. The palladium clusters encapsulated in the MOF act as catalysts for the Buchner ring expansion reaction. Remarkably, **3** exhibits high catalytic activity and reusability, resulting in a turnover number (TON) of above 2000, which is significantly superior to the state-of-the-art catalyst $Rh_2(OAc)_4$ (TON = 104).[39] The catalytic activity of compound **3** also outperforms the catalysts that are used for carbene-transfer-mediated reactions of diazo compounds with some TON values up to 100,000.

In 2019, Zhou and co-workers synthesised metal clusters in HUST-1 MOF *via* the postsynthetic metalation (PSM) method.[23] HUST-1 was synthesised by reacting HUST-1 (Fig. 3a) with nickel halides the authors were able to demonstrate the formation of

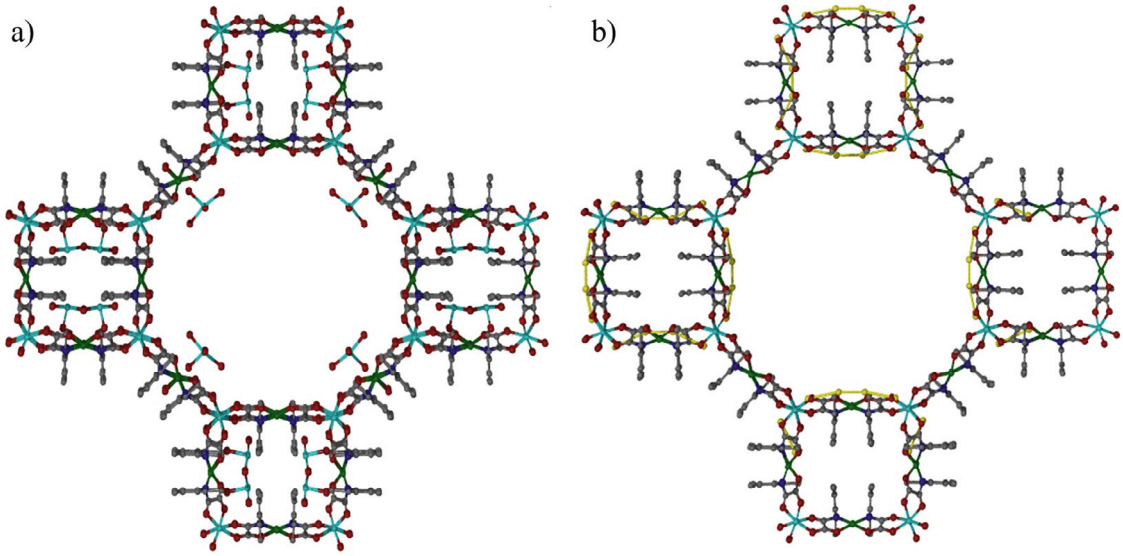

Fig. 2. Single crystal structures of a) **2** and b) **3** viewed down the pores. Gray: C. Red: O. Light blue: Ni. Dark green: Cu. Dark blue: N. Yellow: Pd. H atoms omitted for clarity. [38].

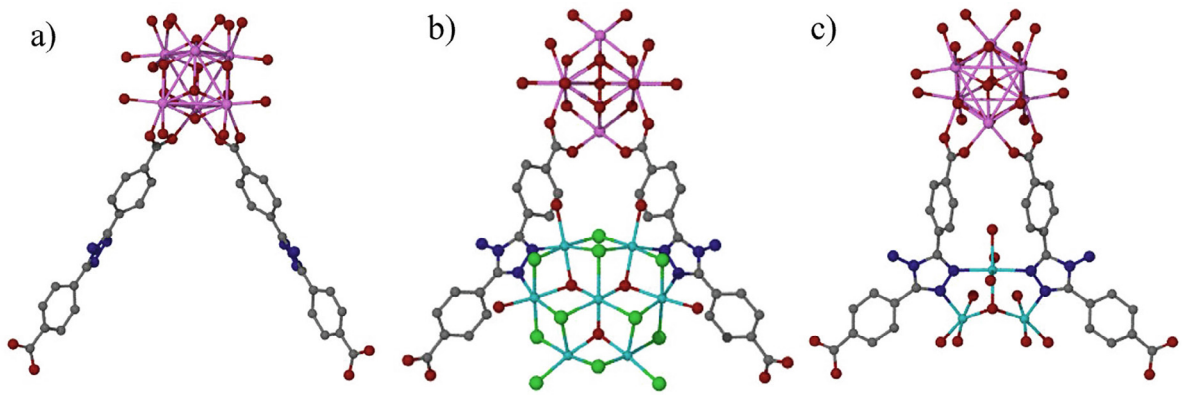

Fig. 3. Crystal structures of a) HUST-1, b) HUST-2 and c) HUST-3. Red: O. Gray: C. Dark blue: N. Light blue: Ni. Light green: Cl. Pink: Zr. H atoms omitted for clarity.[23].

trinuclear (HUST-3) and heptanuclear (HUST-2) nickel clusters inside the pores by SXRD (Fig. 3b and c). Nickel ions were also successfully incorporated into the pores of HUST-1, but the characterisation *via* SXRD was unsuccessful. The nickel-incorporated MOFs have been used as heterogeneous catalysts for ethylene dimerization. Due to their larger pores, the HUST-series catalysts showed higher catalytic activity and superior butene selectivity than the nickel-containing UiO-67 MOF. Within the HUST-series, HUST-3 exhibits the highest activity toward butene production because nickel centres in the trinuclear clusters have more unsaturated metal sites.

The main disadvantage of the HUST-series MOFs is the inability to control the size and shape of the metal clusters. Long and co-workers have reported a method to prepare two-dimensional metal sheets inside the MOF $Zr_6O_4(OH)_4(bpydc)_6$ (bpydc = 2,2′-bi pyridine-5,5′-dicarboxylate) with the ability to control the size, structure and spatial arrangement of the metal(II) halide sheets. [24] Coordination of the bipyridine organic linkers results in the latter pointing toward the pores of the MOF, facilitating the growth of metal halide sheets. Magnetic susceptibility studies showed that the iron halide sheets exhibit superparamagnetism below 8 K, a phenomenon not observed for bulk iron chloride. This work highlights the ability to control the design of the structures and sizes of metallic clusters inside MOFs, which can be used to synthesise a variety of metal NPs for desired applications.

POMs are a type of metal–oxygen clusters with well-defined topologies and diverse structures and potential applications in catalysis and medicine.[40,41] Liu and co-workers have reported on the encapsulation of a polyoxometalate (POM) cluster $LaW_{10}O_{36}$ cluster inside the pores of MIL-101(Cr).[42] The mesoporous cages of MIL-101(Cr) were filled with LaW_{10} *via* a tandem post-synthetic modification of the MOF by stirring the evacuated MOF in a solution of the polyoxometalate yielding LaW_{10}@MIL-101 material. X-ray fluorescence spectroscopy and inductively coupled plasma optical emission spectroscopy show a homogeneous dispersion of $LaW_{10}O_{36}$ inside both smaller (25 Å diameter) and larger (29 Å diameter) MOF cages. Pyridine-adsorbed IR spectroscopy (Py-IR) can be used to characterise coordinatively unsaturated metal sites by exposing the material to pyridine vapour and subsequently recording its FT-IR spectrum. Py-IR shows that the oxygen atoms of the POM cluster interact with the unsaturated Cr^{3+} metal sites. This is further supported by XPS analysis, in which shifts in the La_3d and Cr_2p spectra correspond to the formation of W═O···Cr coordination bond, which is attributed to the confinement effect of the MIL-101(Cr) framework. The LaW_{10}@MIL-101 acts as a catalyst for oxidative desulfurization of benzothiophene (BT), dibenzothiophene (DBT) and 4,6-dimethyldibenzothiophene (4,6-DMDBT). The catalytic efficiency of LaW_{10}@MIL-101 after 180 min of reaction time is 99.1 %, 94.5 % and 87.4 % for DBT, 4,6-DMDBT and BT, respectively. The catalytic efficiency toward desulfurization of BT and 4,6-DMDBT is the highest reported, along with nearly full desulfurization of DBT (although 100 % catalytic efficiency has been reported elsewhere using a similar method of encapsulating POMs in the MIL-101(Cr) framework). Crucially, however, the catalyst can be reused at least seven times without losing significant activity although a small decrease from 98.2 % to 96.8 % for DBT conversion after 120 min reaction time is observed. This remarkable stability is attributed to the W = O···Cr coordination bond which anchors the catalyst to the pore, thus preventing leaching.

Wöll and co-workers have encapsulated $Au_{55}(PPh_3)_{12}Cl_6$ clusters inside surface-supported MOF (SURMOF) thin films Cu-QPDC (**4**) and Cu-PPDC-CH_3 (**5**).[43] Both **4** and **5** are synthesised onto a hydroxyl-functionalised Si substrates using a layer-by layer method. First, a layer of compound **4** or **5** is sprayed onto the film, followed by a loading of the clusters onto the MOF layer and subsequent spraying of the next MOF layer. This process is repeated until a sandwich-like structure of **4** and **5** containing $Au_{55}(PPh_3)_{12}Cl_6$ clusters is obtained. Quartz crystal microbalance (QCM) measurements reveal that the loading efficiency of Au_{55} clusters is around 25 %. Experimentally obtained PXRD patterns of compound **4** fully loaded with $Au_{55}(PPh_3)_{12}Cl_6$ clusters reveal a substantial decrease in the 001 peak compared to the empty **4** indicating successful encapsulation of the gold clusters. However, computational modelling using density functional theory (DFT) showed a significantly stronger intensity of the 001 reflection compared to that of the experimentally obtained. Thus, ligand-stripped Au_{55} clusters were placed inside the pore of **4** and allowed to move freely in order to systematically search for the best theoretical match between the experimentally and theoretically obtained peak intensities. A good agreement is obtained for a structure in which the Au_{55} clusters are positioned in the corners of the pores of **4**. The stripping or partial displacement of PPh_3 ligands is a result of a competitive binding site which stabilises the Au_{55} cluster inside the pores of **4**. The catalytic efficiency of the gold nanocluster encapsulated inside **4** was evaluated by 4-nitrophenol reduction reaction. UV–vis absorption spectra show that Au_{55}@**4** exhibits superior reduction of 4-nitrophenol to 4-aminophenol compared to bulk $Au_{55}(PPh_3)_{12}Cl_6$.

Heavy metal pollution in water has significant negative impacts on animal and human health, ranging from carcinogenic effects to liver damage and cerebral disorders.[44] Chromium(VI) is a highly toxic heavy metal and is more toxic compared to Cr^{III} and Cr^{VI} often exists as a chromate or dichromate oxyanion.[45] In 2020, Li and co-workers synthesised zirconium- and hafnium-based

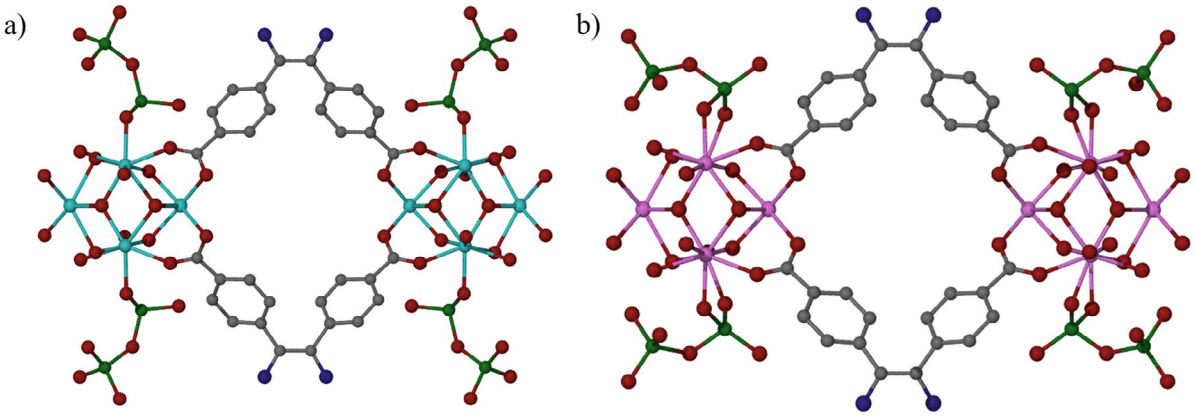

Fig. 4. Single crystal structures of a) Hf-MOF-2 with $Cr_2O_7^{2-}$ anions viewed along the 001 axis and b) Zr-MOF-2 with $Cr_2O_7^{2-}$ anions viewed along the 001 axis. Gray: C. Red: O. Light blue: Hf. Pink: Zr. Green: Cr. Hydrogen atoms omitted for clarity.[46].

isostructural MOFs (Zr/Hf-MOF-1, Zr/Hf-MOF-2 and Zr/Hf-MOF-3) for the detection of $Cr_2O_7^{2-}$ in aqueous solutions.[46] UV–vis absorption spectra show that Hf-MOF-2 has the highest maximum capture capacity of $Cr_2O_7^{2-}$ out of the synthesised MOFs. In addition, Hf-MOF-2 which has a neutral framework outperforms other reported cationic MOFs such as FIR-53 and 1-Br.[47,48] Luminescence quenching efficiency is the highest for Zr/Hf-MOF-3, which also have a limit of detection of 0.013 and 0.019 μM, respectively. These values are similar to the best performing MOFs reported. SXRD analysis of the $Cr_2O_7^{2-}$-loaded Hf-MOF-2 is shown in Fig. 4. This reveals that $Cr_2O_7^{2-}$ clusters replace the H_2O/OH^- groups coordinated to the Zr_6 or Hf_6 clusters of the MOFs. In addition, the enhanced pore size of the isostructural Zr/ Hf-MOF-2 compared to Zr/Hf-MOF-1 and -3 allow for two more $Cr_2O_7^{2-}$ anions to bind inside each pore. This is the first time $Cr_2O_7^{2-}$ anions have been characterised inside MOF pores by SXRD and confirmed the hypothesis that the uptake mechanism of the anion proceeds by coordinating to the SBU oxide clusters.

2.2. Organic clusters

The crystalline sponge method (CSM) allows the determination of the structure of guest molecules encapsulated in the pores of a single crystal of a porous coordination network. The advantages of this method are that the guest molecules do not have to be crystalline to allow inclusion and crystal structure determination, and only a trace amount (<0.1 μg) of the guest is required. CSM was originally introduced by Fujita and co-workers who determined the structures of a variety of guest molecules encapsulated in the pores of single crystals of $\{[(ZnI_2)_3(TPT)_2]_x(solvent)\}_n$ MOF (**6**) (TPT = 2,4,6-tris(4- pyridyl)-1,3,5-trazine).[32] The absolute structures of chiral molecules, such as santonin and myakosine A were successfully determined. In fact, this is the reported crystal structure of myakosine A. In addition, the slow diffusion of guest compounds into the pores of the MOF results in well-ordered structures making CSM a very attractive method to study confined molecular clusters.

In 2016, Fujita and co-workers closely examined the steps involved in CSM and analysed the advantages and disadvantages of various guest soaking methods, such as the original, a-grain-of-crystal, slow evaporation and high-throughput.[49] Fujita and co-workers also expanded on factors that affect crystallographic analysis such as guest occupancy, molecular recognition sites, data collection conditions and structure refinement. For instance, the authors recommend using Cu Kα radiation for diffraction data collection as it yields higher I/σ values for high-angle regions compared to Mo Kα radiation. Overall, this work provides optimized steps for reliable and reproducible X-ray crystallographic analysis of guest molecules when undertaking CSM, a very attractive method for the determination of absolute configuration of a wide array of compounds.

The main drawback of MOF **6** in the CSM context is the hydrophobicity of the pores which means that most of the guest molecules that can be encapsulated are hydrophobic. In addition, **6** is not stable in many solvents. These drawbacks were remedied by the synthesis of the novel RUM-series MOFs (RUM-1, RUM-2 and RUM-3) based on f-block metals.[50] RUM-1 and RUM-2 are synthesized using 1,3,5-benzenetribenzoic acid (H_3BTB) and differ only by the connectivity of the organic linker to the secondary building units containing gadolinium. The framework in RUM-1 is two-dimensional while RUM-2 is three-dimensional. RUM-3 employs the 4,4′,4′′-(1,3,5-triazine-2,4,6-triyl)tribenzoic acid (H_3-TATB) linker connecting cerium or dysprosium. RUM-1 and RUM-2 are the most stable MOFs in the series, and both are stable in a variety of polar solvents. Due to the microporous size of the MOFs cavities, only small organic molecules such as carvone, ε-caprolactam and pyridine can be encapsulated. This work established the capability of CSM to be successfully applied using various solvents and overcoming hydrophobicity by hydrogen bond interactions *via* water molecules coordinated to the secondary building unit metals in the case of RUM-1 and vacant metal sites in the case of RUM-2 and RUM-3.

However, the CSM concept can also work without using any solvent (*i.e.* without soaking MOF single crystals in a solvent in which the target guest is dissolved). In 2018, Eddaoudi and co-workers reported on the synthesis of a novel Cr-soc-MOF, which is capable of capturing twice its own weight of water (1.95 g g^{-1}).[22] Cr-soc-MOF contains channels of roughly 17 Å and cages of roughly 15 Å in size. SXRD analysis of this material after water adsorption reveals that 114 water molecules form a cluster inside the cages (Fig. 5). The encapsulated water molecules form hexamers and heptamers which interact more strongly with each other rather than with water molecules located on the cage edges. This suggests that some water molecules could be acting as nuclei to form aggregates of hexamers and heptamers. Furthermore, if nucleation processes are possible in these systems, they could also be used as vessels for nanosized crystallization.

In order to study how confined water clusters behave in a hydrophobic environment, Kitagawa and co-workers synthesised a metal–organic square-shaped nanotube **7** (Fig. 6).[51] Compound

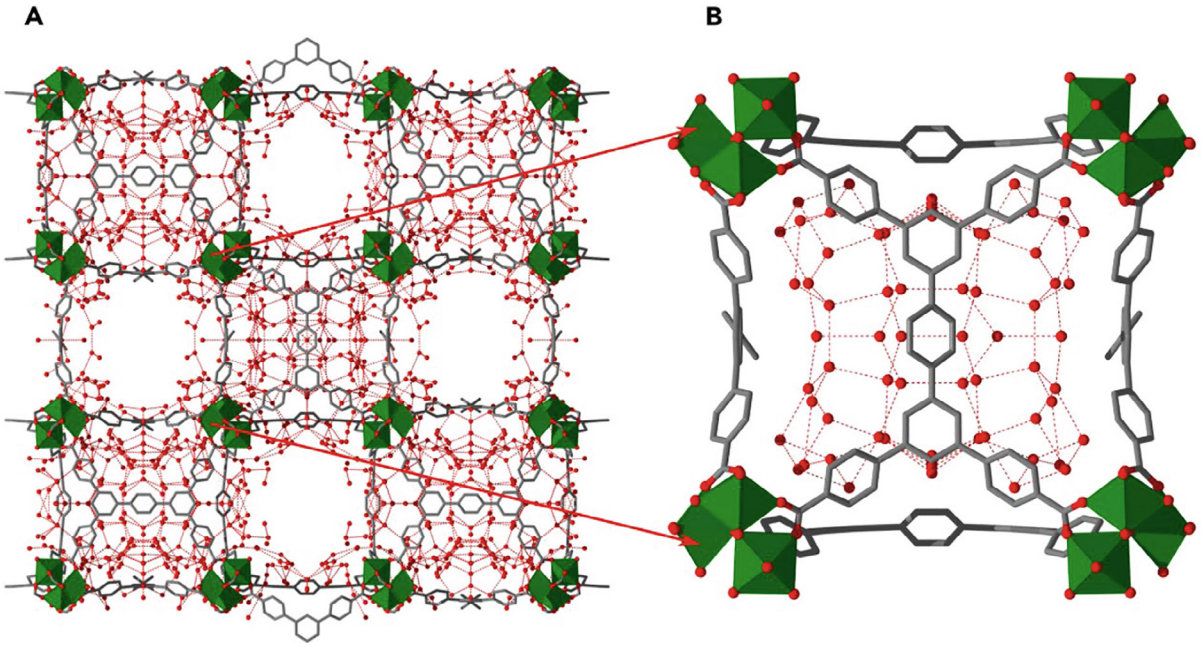

Fig. 5. a) Single crystal X-ray diffraction analysis of the channels and cages of water-absorbed Cr-soc-MOF. b) Position of water molecules inside the cage of Cr-soc-MOF. Hydrogen atoms have been omitted for clarity.[22].

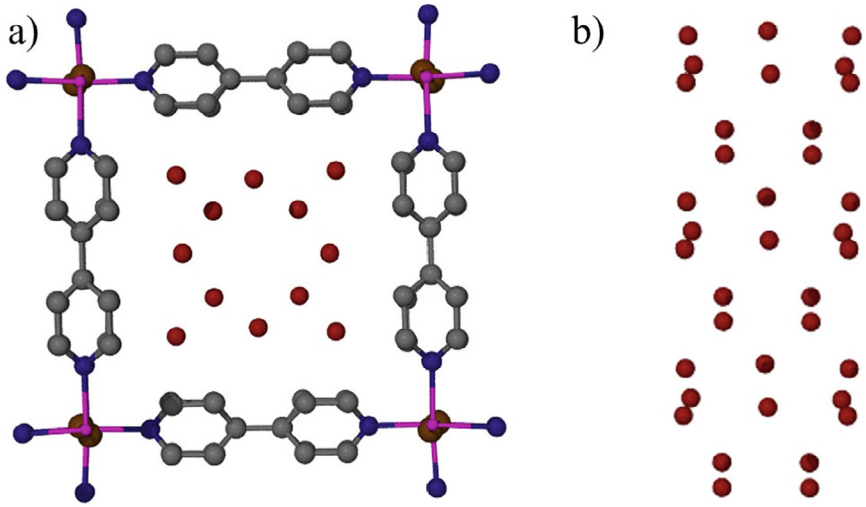

Fig. 6. a) View down channel A of **7** showing the water oxygen atoms and b) Side view of the octa- and tetranuclear water clusters inside channel A of **7**. Gray: C. Dark blue: N. Purple: Pt. Brown: Br. Red: O.[51].

7 contains two channels; the larger channel A is hydrophobic and smaller channel B is hydrophilic. Inside channel B, water clusters form a hydrogen-bonding network with the terminal amino groups and sulfate anions. However, water clusters in channel A are vastly different. Inside the hydrophobic channels, there are two types of water clusters, tetramers and octamers. The O—O distances are in the range of 2.5–2.7 Å, corresponding to strong hydrogen bonding between water molecules in clusters. In addition, in the *a*-direction, the clusters also form weaker hydrogen bonds as the O—O distances vary from 3.0 to 3.4 Å.

Comparing the pores of Cr-soc-MOF and nanotube **7** can provide insight into what nanoconfinement effects promote the formation of these specific clusters. For example, there is a slight difference in pore sizes; the size of Cr-soc-MOF cage is 15 Å while the nanotube channel is 14 Å in size. Intuitively, it would expected that larger clusters are formed inside Cr-soc-MOF pores. However, the largest cluster of water molecules consist of heptamers (7 molecules) inside Cr-soc-MOF while octamers (8 molecules) form inside the smaller nanochannel. This implies that the pore geometry plays an important role in the nucleation processes. Indeed, the shape of these voids are drastically different. The endless rectangular channels of the nanotubes result in the formation of two-dimensional water cluster layers of tetramers and octamers, which are relatively planar and form rectangular-shaped clusters. In the case of the cage, the clusters are not layered and rather form three-dimensional clusters. The cages of Cr-soc-MOF rather consist of water hexamers and heptamers inside the cages with single water molecules on the side of the cages, as Eddaoudi and co-workers propose, acting as nuclei. In terms of intermolecular interactions between the frameworks and guest clusters, both

Cr-soc-MOF and nanotube material **7** contain hydrophobic voids. Thus, it is more likely that water clusters assemble *via* hydrogen bonding interactions and take up clusters that have a good fit within the pores. Kitagawa and co-workers add that the clustering of water molecules arises from the hydrophobic nature of the channels, an effect similar to that observed in carbon nanotubes and ion transport proteins.[51–54].

Recently, Yaghi and co-workers combined DFT calculations with experimental crystallographic structures to reveal the evolution of water clusters inside MOF-303.[26] MOF-303 is composed of 1-*H*-pyrazole-3,5-dicarboxylate (H_2PZDC) linkers connected together by AlO_6 secondary building unit clusters and exhibits the **xhh** topology. MOF-303 is efficient in capturing water (0.48 g g^{-1}) and the water sorption isotherm reveals a three-step adsorption process. Thus, single crystals were synthesised to study-one-by-one nucleation of water molecules inside MOF-303. Synchrotron SXRD analysis reveals the locations of the first four adsorbed water molecules. The first two water molecules are located between two pyrazole units, which is also the most hydrophilic part of the framework. The third and fourth water molecules interact with the μ_2-OH group and the first two water molecules, respectively. The subsequent nucleation of water molecules onto the "seed" of the first four was investigated *via* DFT calculations. The results reveal that the nucleated water molecules interact with previously bound water molecules rather than with the surrounding MOF. The addition of fifth and sixth water molecules results in the formation of a tetramer cluster, which is transformed into a hexamer by the addition of seventh and eighth water molecules. The addition of water molecules 5–8 signifies the second step in the isotherm and is referred to as the clustering phase. In the final networking phase, water molecules 9 through 14 partly fill the MOF pores to form permanent H-bonded water chains throughout the framework pores, resulting in the total uptake of 0.45 g g^{-1}, which agrees with the experimentally obtained water isotherm. Additionally, the authors replaced the $PZDC^{2-}$ linkers with 2,4-furandicarbopxylic acid to probe the importance of the hydrophilic pocket presented by the $PZDC^{2-}$ linker towards the efficient seeding of water molecules. It was found that the initial water molecules bind to the μ_2-OH sites rather than the organic linker sites.

In 2018, Pardo and co-workers isolated single platinum metal ions stabilised by a water cluster inside the pores of a mesoporous MOF.[55] The authors synthesised a nickel-based MOF having the formula $Ni^{II}_2\{Ni^{II}_4[Cu^{II}_2(Me_3mpba)_2]_3\}\cdot 54H_2O$ (**8**) (Me_3mpba = N,N'-2,4,6-trimethyl-1,3-phenylenebis(oxamate)), which was subsequently treated with $[Pt(NH_3)]^{II}_4$ to yield $[Pt^{II}_2(m\text{-}OH_2)(NH_3)_6)]_{0.65}[Pt^{II}(NH_3)_4]_{0.7}\{Ni^{II}_4[Cu^{II}_2(Me_3mpba)_2]_3\}\cdot 65H_2O$ (**9**) and $NaBH_4$ to yield $[Pt^{II}_2(\text{-}O)(OH)_2(NH_3)_4]_{0.5}Pt^{I}@Na_3\{Ni^{II}_4[Cu^{II}_2(Me_3mpba)_2]_3\}\cdot 79H_2O$ (**10**). XANES analysis of framework **10** suggests that the encapsulated platinum ions are oxidised and exhibit a different local environment compared to platinum foil. Furthermore, EXAFS spectra indicate the presence of Pt–O or Pt–N bonds and a high dispersion of platinum ions in the framework of **10**. Indeed, SXRD analysis of the framework shows that platinum ions are coordinated to four water molecules and the cluster is stabilised by hydrogen bond interactions between the water molecules and the framework ligands. DFT structure of platinum ions inside the pores of **10** also suggests the presence of a second coordination sphere, which consists of three water molecules interacting with the platinum–water cluster and the framework *via* hydrogen bonding. Thus, the pore acts as a confinement matrix to stabilise the platinum metal and the surrounding water clusters. Subsequently, **10** was used as a catalyst for the water–gas shift reaction, which generates CO_2 and H_2 from carbon monoxide and water, generally by using platinum or gold ions as catalysts. The catalytic activity of **10** was compared to other Pt-supported catalyst and remarkably **10** shows the highest activity up to 150° C. Pardo and co-workers suggest that the mechanism of CO_2 formation stems from the encapsulated water molecules, which trigger a double water attack on the CO to yield CO_2 at temperatures as low as 50 °C. This superior activity compared to other Pt-supported catalysts arises from the confinement effect of the pore which stabilises the Pt^{I} ions and its surrounding water clusters. The presence of Pt^{I} rather than Pt^{II} or Pt^{0} was confirmed by X-ray photoelectron spectroscopy.

Overall, these results suggest that MOFs can be designed for selective binding of guest molecules. More importantly, the close agreement between SXRD measurements and DFT calculations for the seeding event inside the MOF suggests that the shape and environment of MOF pores leads to a specific arrangement of water molecules unique to that MOF. In other words, water molecules assemble to unique polymorphs inside different MOFs. This concept could potentially be applied to crystallize novel polymorphs of small organic molecules inside MOFs by gaining control over the seeding and clustering pathways to form an initial nucleus of critical size, which would subsequently direct the crystal growth phase. So far in this work, various water clusters have been observed for both hydrophilic and hydrophobic MOF pores. The evidence suggests that designing hydrophilic MOF pores could be advantageous in terms of controlling where the initial guest seeds form. Subsequently, using computational modelling, the shape of the corresponding guest nuclei could be predicted to obtain clusters, and eventually polymorphs, with the desired shapes and properties.

2.3. Solid-state clusters of gases

The efficient capture and storage of greenhouse gases, such as carbon dioxide, methane and chlorofluorocarbons, is a global ambition due to the negative effects of their presence in the atmosphere. Carbon dioxide is the most commonly produced greenhouse gas and subsequently much research is focused on its sequestration. MOFs provide well-defined pores (in the form of cages and channels) that can be used for gas capture and storage. This process is generally performed in the solid state under high pressure and a flow of gas. Thus, MOFs that retain their crystallinity under these conditions are highly sought after, because subsequent analysis *via* SXRD can provide insights into how the gas molecules order inside the pores. Additionally, this aids in the future design of MOFs for the efficient sequestration of desired gases. However, the encapsulation of gases is best studied *via* sorption isotherm experiments. Upon gas sorption, crystalline MOF structures generally lose their crystallinity, *i.e.* they are no longer suitable for SXRD analysis. As a result, there is a relatively limited literature on crystal structures of MOFs containing solid-state nanoclusters of gas molecules.

The earliest report containing direct observation of gas molecules inside a MOF is from 2005 by Kobayashi and co-workers.[56] A pillared layer coordination polymer CPL-1 with microporous channels of 4 × 6 Å was synthesized and used for hydrogen adsorption studies. Synchrotron PXRD analysis of empty CPL-1 at 90 kPa and hydrogen-adsorbed CPL-1 (H_2@CPL-1) at 102 kPa were analysed using the maximum entropy method (MEM)/Rietveld method to determine the single crystal structures. The MEM charge-density distribution maps of H_2@CPL-1 show electron density corresponding to two hydrogen atoms inside the channels of the framework. The H_2 atoms are slightly displaced from the centre of the pores, closer to the oxygen atoms of the carboxylate group of the organic linker pyrazine-2,3-dicarboxylate.

In 2010, Takeda and co-workers synthesised a series of metal–organic one-dimensional assemblies to study the adsorption of CO_2, H_2, N_2, O_2 and Ar.[57] Single crystalline hosts $[M^{II}_2(bza)_4(\text{-}Rpyz)]_n$ (bza = benzoate, pyz = pyrazine, M^{II} = Rh^{II} (**a**) or Cu^{II} (**b**), *R* = H (**11**), 2-methyl (**12**) or 2,3-dimethyl (**13**)) were synthesised

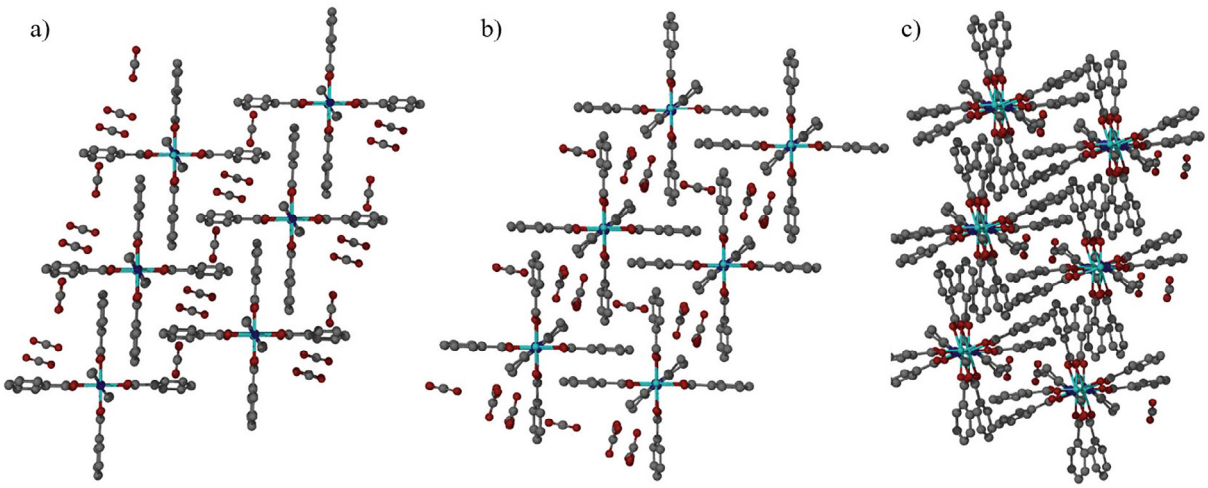

Fig. 7. Single crystal structures of CO_2-absorbed metal–organic assemblies viewed down the pore axis. a) **11a**, b) **12a** and c) **13a**. Red: O. Gray: C. Light blue: Rh. Hydrogen atoms have been omitted for clarity.[57].

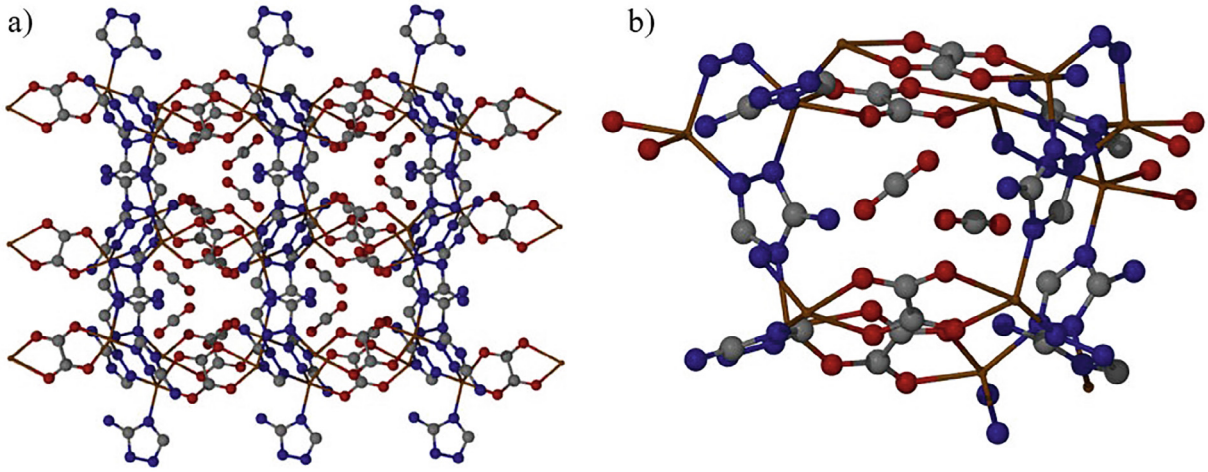

Fig. 8. Binding of CO_2 inside the micropores of $Zn_2(Atz)_2(ox)$ as determined *via* SXRD. a) Unit cell packing of $Zn_2(atz)_2(ox)$ in the *b* axis. b) Two crystallographically unique CO_2 molecules inside the cage of $Zn_2(Atz)_2(ox)$. Red: O. Gray: C. Blue: N. Hydrogen atoms have been omitted for clarity.[59].

via vapour diffusion and adsorption experiments were carried out under 195 K for CO_2 and 77 K for other gases under varying pressure conditions. For **11**, **12**, and **13**, the maximum absorption capacity of CO_2 is 3 molecules per M_2 unit for **11** and **12** and 2 molecules for **13**. Single crystal structures of **11a**, **12a** and **13a** after CO_2 absorption studies are shown in Fig. 7. The single crystal structures of CO_2-loaded **11a**-**13a** are isostructural to those of **11b**-**13b** and thus only structures **11a**-**13a** are shown here. The guest-absorbed **12a** undergoes a pore expansion to accommodate three CO_2 molecules per M_2 unit. The encapsulated CO_2 molecules are arranged in a A–A–B type as seen in Fig. 7a. The parallel arrangement for A–A CO_2 molecules is the most stable arrangement of that two CO_2 molecules can undertake while the perpendicular A–B is the second most stable.[58] Fig. 7b shows that the crystal structure of **12a** still contains three CO_2 molecules despite the addition of a methyl group onto the pyrazine ring. A similar structural transformation in which the pore size increase is observed for the CO_2-absorbed **12a** compared to its empty counterpart. In addition, the as-synthesised **12a** exhibits zigzag-like pore structure and upon CO_2 inclusion the shape of the pores changes to a one-dimensional straight pore with a similar A–A–B type packing of the guest molecules. Fig. 7c shows the CO_2 inclusion structure of **13a** which contains the 2,3-dimethylpyrazine organic linker, thus adding an extra methyl group per linker into the pores compared to **12a**. The structure reveals a significant reduction in the number of encapsulated CO_2 molecules, from 3 to 0.49 per M_2 unit. The addition of a methyl group prevents the structural transformation that was observed in the case of **12a** and the host remains in a zigzag-like arrangement. Overall, Takeda and co-workers conclude that controllability of the dynamic adsorption properties of host molecules can lead to novel diffusivity and dynamic selectivity of guest molecules inside this type of flexible porous hosts.

In 2010, Woo and co-workers reported a microporous amine-based MOF $Zn_2(atz)_2(ox)$ (atz = 3-amino-1,2,4-triazole; ox = oxalate) which was used for CO_2 capture.[59] Notably, this was the first example of a crystal structure of a CO_2 adsorbed MOF. Crystallographic studies of the CO_2-absorbed MOF samples showed two unique binding sites inside the pores with 80 % and 50 % occupancy. Fig. 8a shows packing of $Zn_2(atz)_2(ox)$ with two CO_2 molecules occupying each pore. One CO_2 molecule binds to the free amine group of atz (Fig. 8b, rightmost CO_2 molecule, CO_2(I)) while the other CO_2 molecule is positioned closer to the ox moiety

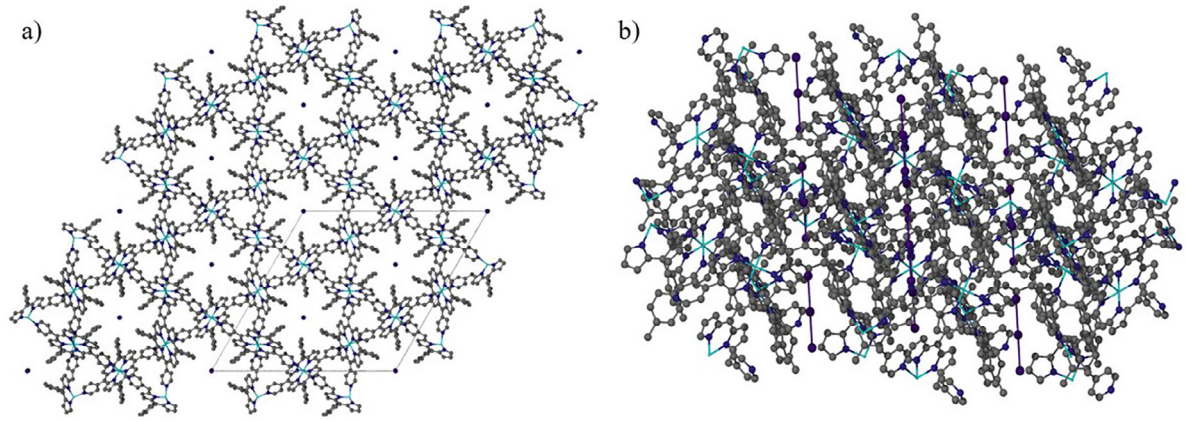

Fig. 9. Polyiodide chains inside the pores of **14**. a) View along the *c* axis. b) View of the polyiodide chains in the MOF pores. Gray: C. Dark blue: N. Light blue: Co. Purple: I. Hydrogen atoms have been omitted for clarity.[60].

(Fig. 8b, leftmost CO_2 molecule, CO_2(II)). The authors demonstrated cooperative binding of the guest molecules *via* SXRD and computational modelling studies. The binding energy for CO_2(II) is 4.6 kJ mol^{-1} higher when its adjacent site is occupied compared to when it is unoccupied by CO_2, determined by dispersion-corrected periodic DFT calculations. Further calculations showed an interaction energy of 3.9 kJ mol^{-1} between CO_2(I) and CO_2(II). The authors suggest that enhancing the pore size could result in significantly higher CO_2 loading capabilities as a result of the cooperative binding.

Iodine and carbon dioxide uptake of a porphyrin-based microporous Co-DpyPtolP-MOF (DpyPtolP = 5,15-di(4-pyridyl)-10,20-di-(4-methylphenyl)porphyrin) (**14**) was analysed in 2015 by Lee and co-workers.[60] Material **14** retains its crystallinity even after vacuum drying at 250 °C to evacuate the solvent molecules. Thus, single crystals of **14** were exposed to CO_2 gas under 195 K and analysed *via* SXRD. The crystal structure of the CO_2-adosrbed framework reveals a linear arrangement of the guest molecules in the one-dimensional pores of the framework. Only a few other examples of solid-state structures of confined CO_2 molecules inside pores or cages have been reported to date.[61,62].

Compound **14** was also used to study the uptake of iodine by immersing the MOF crystals in a cyclohexane solution of iodine. SXRD analysis of the iodine-adsorbed crystals revealed the formation of polyiodide clusters inside the one-dimensional pores (Fig. 9a and b). More specifically, the central iodine atom has an inversion centre and symmetry expansion generates a I_3^- ion. The $I_3^-\cdots I_3^-$ distance inside the channel is 3.212 Å, which is significantly shorter than the distance of $I_3^-\cdots I_3^-$ chains previously determined in [H_3O(dibenzo-18-crown-6)] at 4.0–4.2 Å.[63] The authors conclude that instead of discrete I_3^- ions, the iodine atoms form a symmetric structure inside the framework pores because the exact identity of the polyiodide clusters is different from pure I_2 or I_3^-. Raman spectroscopy analysis of encapsulated polyiodide clusters showed different signals compared to those of pure I_2 or I_3^-. The latter exhibit signals at 200, 170 and 103 cm^{-1} while polyiodide clusters give new signals at 333, 220 and 161 cm^{-1}. This unique behaviour of iodine in this system in which it does not resemble either I_2 or I_3^- has not been previously observed and could potentially be driven by the geometry of the pores of **14**. Previously in 2008, I_3^- species were encapsulated into two indium-based MOFs with tetratopic tetrathiafulvalene linkers.[64] However, in this case the formation of I_3^- was directly confirmed *via* SXRD as the latter act as counterions for the reduced organic linkers.

In 2018, Miyasaka and co-workers used a framework-like porous layered ferrimagnet [{Ru^{II}(3,5-F_2PhCO_2)$_4$}$_2${TCNQ(MeO)$_2$}]·3(DCM)·1.5(DCE) (**15-solv**, 3,5-F_2PhCO_2 = 3,5-difluorobenzoate, TCNQ(MeO$_2$) = 2,5-dimethoxy-7,7,8,8-tetracyanoquinodimethane, DCM = dichloromethane and DCE = dichloroethane) for gas sensing applications.[65] As-prepared **15-solv** has inter-layer distance of 9.78 Å which contracts to 9.46 Å upon the release of DCM and DCE (**15**), a reversible process when reintroduced to vapours of DCM and DCE. Adsorption isotherms of O_2, N_2 and CO_2 show that **15** is capable of encapsulating these gases. *In situ* SXRD analysis reveals the structures of CO_2– and N_2-adsorbed **15** (**15** ▫ CO_2 and **15** ▫ N_2). Adsorption of O_2 was measured at 94 (**15** ▫ O_2-I) and 130 K (**15** ▫ O_2-II, structure solved using the Rietveld refinement technique) due to two gas-adsorbed temperature-dependent phases existing at those temperatures. Thus, *in situ* SXRD was employed at those temperatures as well. All structures containing gas guest molecules exhibit further inter-layer distance decrease from the solvent evacuated **15**. The structures of **15** ▫ N_2 and **15** ▫ O2-II are almost identical and their occupancy numbers are 4 and 5.2, respectively while that of **15** ▫ CO_2 is 5.0. The smaller occupancy of N_2**@15** leads to the framework having the shortest interlayer distance of 8.76 Å while **15** ▫ CO_2 and **15** ▫ O_2-II exhibit nearly identical distances of 9.11 and 9.10 Å. Magnetic measurements of **15** ▫ CO_2 and **15** ▫ N_2 show an increase in the Curie temperature (T_C) relative to **15**. This change in T_C is likely the result of a reduction in structural deformation that **15** exhibits upon transformation from **15-solv** to **15**, *i.e.* the structural deformation upon gas adsorption results in a structure more similar to **15-solv** than **15**. Magnetic measurements were repeated for **15** ▫ O_2, which is a paramagnetic gas unlike CO_2 and N_2. Upon O_2 adsorption, the resulting material exhibits antiferromagnetic (AF) properties because O_2 molecules mediate a transition to the AF state *via* intercalated O_2 spins. In short, by introducing O_2 gas into the pores of the ferrimagnet **15**, Miyasaka and co-workers demonstrate facile and fast switching between a ferrimagnet (evacuated **15**) and antiferromagnet (O_2-adsorbed **15**).

In 2021, Miyasaka and co-workers synthesised a stimuli-responsive D_2A-layered (D = donor and A = acceptor) ferrimagnetic MOF [{Ru^{II}(F$_3$PhCO$_2$)$_4$}$_2$TCNQ(OEt)$_2$]·3DCM (**16**-DCM, $F_3PhCO_2^-$ = 2,4,6-trifluorobenzoate, TCNQ(OEt$_2$) = 2,5-diethoxy-7,7,8,8-tetra cyanoquinodimethane) which turns paramagnetic upon CO_2 absorption.[66] The ferrimagnetic behaviour comes from a one-electron transfer between the donor and acceptor throughout the material in a pattern of $[D–A^-–D^+]_\infty$. Similarly to **15**, MOF **16**-DCM shows reversible solvent absorption–desorption to form DCM-free **16** with thermal stability up to 473 K. CO_2-atmosphere-controlled *in situ* SXRD analysis was performed at pressures of 3 kPa (**16** ▫ CO_2-I) and 100 kPa (**16** ▫ CO_2-II). The single

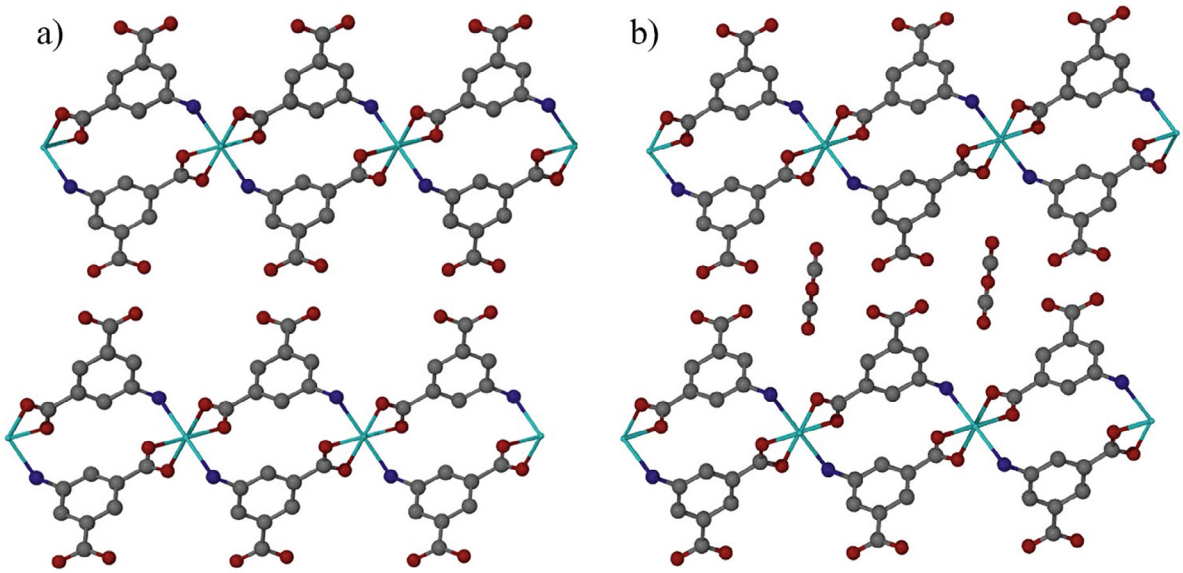

Fig. 10. Single crystal structures of a) MUF-16(Mn) and b) CO_2@MUF-16(Mn) as viewed along the axis of the pores. Light blue: Mn. Gray: C. Red: O. Dark blue: N. Hydrogen atoms have been omitted for clarity.[67].

crystal structure of **16** ▫ CO_2-I reveals a pseudopolymorphic form of **16**-DCM with four molar equivalents of CO_2 replacing DCM molecules in the centre of the MOF pores. However, **16** ▫ CO_2-II crystallizes in a different space group from those of **16**-DCM and **16** ▫ CO_2-I, indicating that the adsorption of CO_2 at 100 kPa induces structural changes of the framework. Indeed, four more CO_2 molecules are encapsulated in **16** ▫ CO_2-II compared to **16** ▫ CO_2-I, resulting in an increase in the void space and flattening of the D_2A layers. Furthermore, the electronic state became neutral for **16** ▫ CO_2-II, which was also confirmed by *in situ* IR spectroscopy showing a broadening and weakening of the $\nu_{C\equiv N}$ band in **16** ▫ CO_2-II compared to **16**-DCM. DFT calculations of different model structures obtained from SXRD analysis show that the neutral ground state of **16** ▫ CO_2-II is the most stable form of the obtained structures, ascribed to a stabilizing interaction between a CO_2 orbital and δ^* orbital of the [Ru_2^{II}] and π^* orbital of TCNQ(OEt)$_2$. Overall, **16** shows reversible ferrimagnetic and paramagnetic behaviour upon CO_2 absorption and desorption. Such gas-responsive materials as **15** and **16** are promising and desired towards applications in gas sensing and capture importantly because of the ability to study structural changes *via* SXRD which is an important tool towards designing future materials for efficient sensing and capture.

Telfer and co-workers reported on the synthesis of a cost-effective MOF series MUF-16 (MUF-16(Co), MUF-16(Mn) and MUF-16(Ni)) to selectively separate CO_2 from hydrocarbons.[67] The MUF-series MOFs exhibit one-dimensional micropores of 3.6 × 7.6 Å and the empty framework is shown in Fig. 10a. The guest gas was introduced to a single crystal of the evacuated MUF-16 (Mn) under 1.1 bar inside a capillary. Fig. 10b shows the single crystal structure the CO_2-adsorbed MUF-16(Mn) with CO_2 molecules packed along the pore axis. The oxygen atoms of CO_2 are involved in hydrogen bonding interactions with the amino (N—H···O) and phenyl (C—H···O) groups at distances of 2.55, 2.81 and 2.87 Å. Based on the occupancy of 50/50 of the guest molecules, this yields the capture capacity of 0.77 molecules per Mn centre, which is in good agreement with the obtained adsorption isotherm. In addition, the encapsulated guest molecules exhibit attractive C···O intermolecular interactions with the distance of 3.78 Å. The combination of these attractive interactions results in strong selectivity of CO_2 towards the pores of MUF-16 MOFs. Separation studies with hydrocarbon mixtures (CO_2/C_2H_6, CO_2/C_2H_4, CO_2/C_2H_2 and CO_2/CH_4) show that hydrocarbons break through from the column at an early stage due to efficient adsorption of CO_2 by the MOF. This results in the productivity of 1 kg of MOF producing 27 L of hydrocarbons from equimolar solutions of CO_2 and hydrocarbon outperforming all previously reported materials. The facile and cost-effective synthesis coupled with excellent selectivity for CO_2 of the MUF-16 series MOFs thus make them a promising physisorbent for CO_2 capture and separation.

Zhou and co-workers reported on the iodine absorption of another redox-active Zr-based MOF with cage sizes in the high microporous (12.6 and 15.8 Å) and low mesoporous (20.6 Å) range.[68] Similarly, I_3^- formed *via* a redox reaction and was relatively easily characterised *via* SXRD. Crucially, the case of Co-DpyPtolP-MOF is rather unique as it is the only known crystalline structure of a chain of polyiodide molecules inside a pore that does not form I_2 or I_3^- species. As observed for water clusters in Cr-soc-MOF and the metal–organic nanotube **7**, voids of different shapes and sizes result in different behaviour of molecules of the same kind. Thus, this warrants reason for further research in the confinement of various molecules in metal–organic-framework-type materials.

3. Nanoconfinement in cages

3.1. Inorganic clusters

In 1991, the Mann group reported on the preparation of iron sulfide nanoclusters inside a ferritin protein cage.[69] *In situ* reaction between iron oxide cores of ferritin and H_2S resulted in the formation of a black solution. Analogous experiments where ferritin was substituted with ferrihydrite suspensions resulted in a similar black discolouration followed by the formation of a black precipitate. This indicates that iron sulfide nanoparticles form inside the cages of ferritin, supported by TEM micrographs showing iron sulfide clusters with mean sizes of 6.8 and 7.8 nm. In addition to iron sulfide, manganese and uranium oxo-species were also successfully synthesised inside the cages. This work showed that it is possible to use large protein cages as confinement matrices for the purpose of synthesising inorganic materials. In 2010, Ceci and co-workers solved the crystal structure of silver-containing

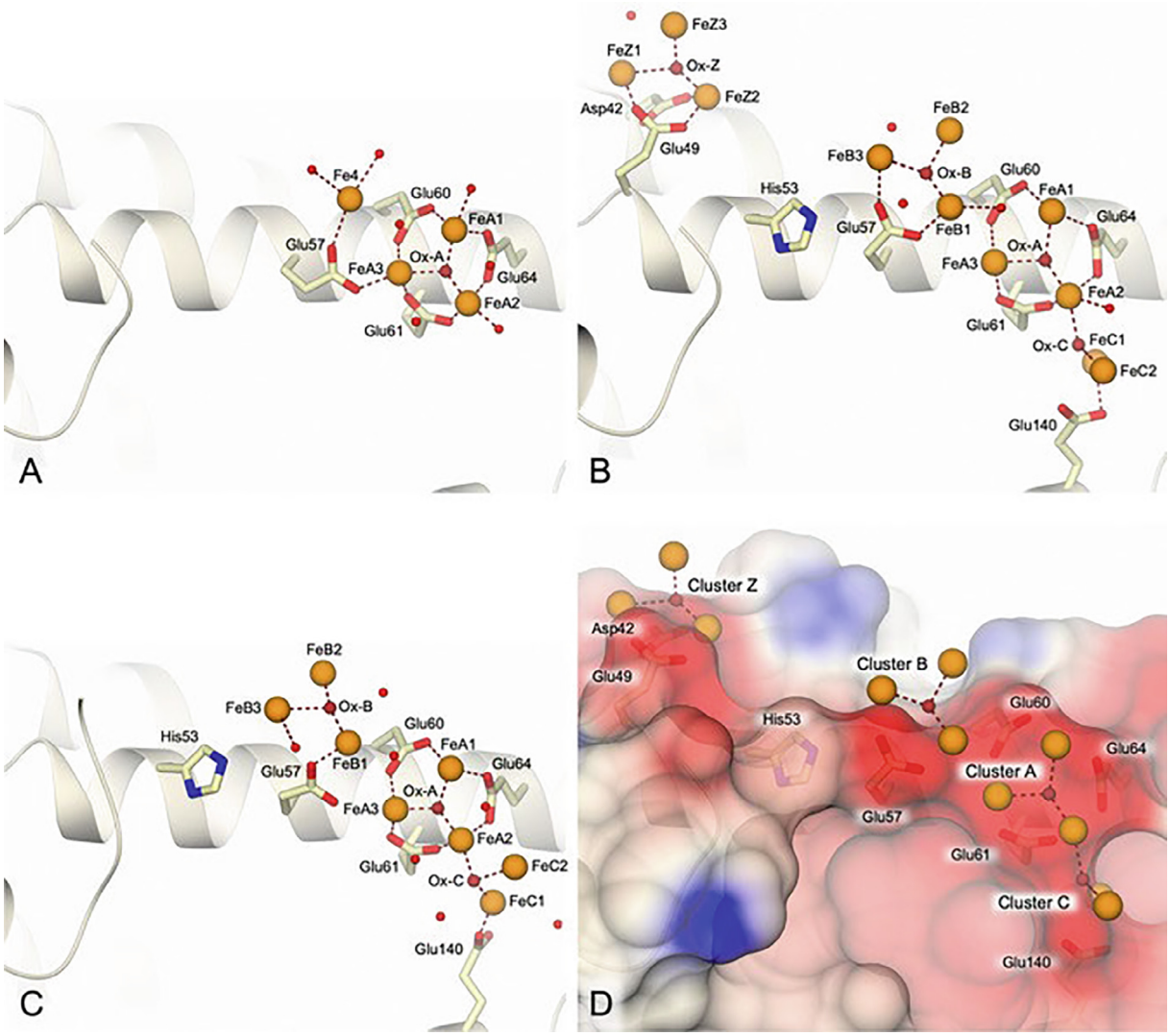

Fig. 11. Single crystal structures of human L-ferritin containing Fe^{III} clusters at A) 15 min, B) 30 min and C) 60 min after Fe^{III} diffusion. D) Electrostatic surface image of iron clusters after 30 min of Fe^{III} diffusion.[25].

P. furiosus ferritin.[70] Notably, this is the first reported crystal structure of ferritin. The authors speculate that the successful loading of silver ions into the protein cage increased the stability of the protein, resulting in its successful crystallization. The crystal structure revealed two unique silver nucleation sites which are likely responsible for the formation of silver nanoclusters with sizes of 2.1 ± 0.4 nm inside the protein pores. The authors conclude that thanks to the high loading of silver NPs, these ferritin-type systems can be used to target silver-based therapies and manufacturing of NPs using thermostable ferritin proteins.

Iron biomineralization in ferritin cages is dependent on the ratio of H- and L- subunits, which self-assemble to form the cage structure of ferritin. H-subunits contain a ferroxidase site which acts as an oxidation site to transform Fe^{II} to Fe^{III}, whereas L-subunits lack this feature.[71] However, an atomic-sized view of the mechanism of mineralization wasn't presented until 2020. Turano and co-workers obtained single crystal structures of homopolymeric human L-ferritin and horse spleen ferritin containing octa-nuclear iron clusters.[25] Turano and co-workers had previously reported a Fe^{III} cluster formation inside L-ferritin, but only for the initial nucleation stages and were unable to repeat it for latter stages due to a loss of crystallinity as a result of slow Fe^{II} aqua-ion diffusion and oxidation.[72] A modified experimental procedure is reported to preserve the crystal quality and monitor iron cluster nucleation by directly diffusing Fe^{III} instead of Fe^{II} ions into ferritin single crystals, followed by flash freezing. Fig. 11 shows single crystal structure snapshots at 15, 30 and 60 min after Fe^{III} diffusion obtained *via* synchrotron radiation. After 15 min, a triiron cluster (labelled FeA1, FeA2 and FeA3) forms on the surface of the ferritin cage, a structure similar to what was previously obtained with Fe^{II} diffusion.[72] However, after 30 min an 8-nuclear iron cluster is observed around the original 3-cluster, indicating that it acts as a seed to aid the growth of further iron ion clusters. A similar structure remains after 60 min of diffusion and after 90 min, the crystal quality of the single crystal deteriorates, thus no further analysis *via* SXRD is possible. This single crystal analysis was also repeated for horse spleen ferritin and a similar Fe^{III} cluster was observed after 60 min of diffusion. Substitution of Glu units on ferritin with Ala units results in a single triiron cluster formation after 60 min, indicating that the initial seed shown in Fig. 11A is crucial in further growth of iron clusters. This work highlights the importance and benefits of using SXRD analysis to understand nucleation mechanisms under nanoscale confinement.

Recently, Lu and co-workers reported on the evolution of a gold cluster inside an apo-ferritin cage.[27] The cage of the protein contains two channels connected by highly symmetric 3-fold and

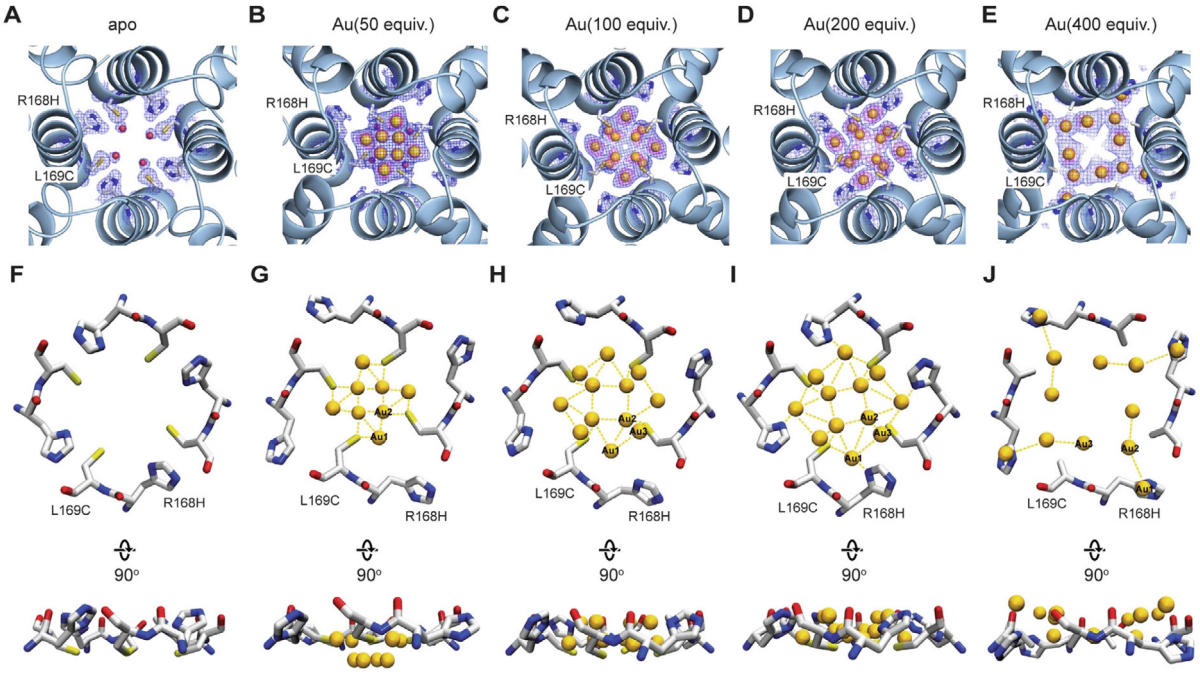

Fig. 12. Electron density maps and crystal structures of metal nanoclusters with varying precursor concentration inside the 4-fold channels. A–E) Electron density maps of the gold nanoclusters. F–J) Crystal structures of the empty channel and gold nanoclusters as viewed along the channel and from the side. The Creative Commons Attribution 4.0 International License can be found at the following link: http://creativecommons.org/licenses/by/4.0/.[27].

4-fold interfaces. The 3-fold channel contains charged Asp122, Asp127 and Glu130 residues, capable of metal ion transportation while the 4-fold channel contains more hydrophobic Leu161, Tyr164, Leu165, Phe166, Leu169 and Leu171 residues. Varying equivalents of the gold precursor chloro(dimethylsulfide) gold(I) was used as the precursor to react with purified protein at pH 8.0 and crystals of the gold-encapsulated protein were obtained *via* the hanging-drop vapour diffusion method. Crystal structure of gold-encapsulated ferritin reveals four binding sites – 3-fold, Cys48, Met96 and 4-fold sites.

The authors studied the clustering mechanism inside the 4-fold channel. Fig. 12A–E show the clusters of Au ions formed over the range of the precursor concentration used. Since the monomer of the 4-fold site contained 2 or 3 gold ions, the fully constructed 4-fold channel has 8–12 ions. Conformational changes in the protein structure are observed when the concentration of the precursor is changed from 50 to 100 equiv. In addition, the number of encapsulated Au ions increases from 8 to 12. Based on the electron density changes, Au1 has the highest binding affinity towards the 4-fold binding site. At the concentration of 200 equiv. the cluster remains structurally similar to that of 100 equiv. However, at 400 equiv. a significant change is observed. At this concentration, the R186H moiety forms a coordination bond with Au1 while the cluster rearranges into a cubic-like structure with four gold atoms on the edge of the structure. The bond lengths between four Au1 atoms and the ferritin ligand moieties at 100 and 200 equiv. structures are 2.02 and 2.08 Å for Au1–N and Au1 – S, respectively. Au1–Au2 and Au1–Au3 distances are 3.14 and 3.59 Å, respectively, suggesting aurophilic interactions between these gold atoms. Furthermore, this suggests that Au1 act as seeds that further gold atoms can coordinate with and form clusters from. Overall, the authors were able to successfully design a coordination site for gold encapsulation inside the apo-ferritin channels. This work shows that it is possible to precisely tune and control the shape and size of gold clusters in nanospaces by changing the concentration of the gold precursor. A similar concentration effect on gold complexes formed with bis(diphenylphosphino)amine ligands was reported in 2020 by Yam and-coworkers.[73].

In 2010, Fujita and co-workers demonstrated that silica nanoclusters can be successfully synthesised in cages *via* the sol–gel condensation method with tetramethoxysilane (TMOS).[74] Two cages with diameters of 4.6 and 6.3 nm were synthesised using linkers containing glucose units, which line the interior of the cages and act as *endo* templates. The spherical pores were treated with 170 and 500 equivalents of TMOS. Successful condensation of silica nanoclusters was confirmed with ^{1}H NMR spectroscopy, X-ray fluorescence and LDI-MS studies. Single crystals of the cage with encapsulated silica clusters were analysed with synchrotron X-ray diffraction. Due to a large unit cell and high disorder, the interior of the cage could not be modelled. Thus, a silica NP consisting of 170 units was computationally modelled and coupled with the crystallographic model. The combined structures indicate that the cage is able to accommodate the silica cluster with a diameter of 2.8 nm. This is supported by TEM images, which reveal an average cluster size of 2.9 nm inside the cage void. This method could further be applied to prepare even smaller NPs of various metal-based analytes which could exhibit even more unique properties compared to their bulk.

Zhang and co-workers used a thioether-functionalised discrete molecular cage (**17**) with the cavity size of 1.8–2.1 nm to template the growth of gold nanoparticles (AuNPs) inside the cage void.[75] The two-phase liquid–liquid approach using tetraoctylammonium bromide as the phase-transfer reagent results in the *in situ* formation of AuNPs inside the cage void (AuNPs**@17**). In the presence of the thioether-functionalised cage, the UV–vis spectrum of AuNPs exhibits a change from two peaks at 250 and 380 nm to a broad shoulder band in 275–381 nm along with an intensity decrease in the 380 nm peak, indicating the formation of AuNPs inside the cage void. TEM images of AuNPs**@17** confirm the formation of AuNPs with an average diameter of 1.9 nm, in good agreement with the cavity size of **17**. Computational simulations were undertaken with varying AuNP radii inside **17** to study the total energy of cage/cage and cage/AuNP

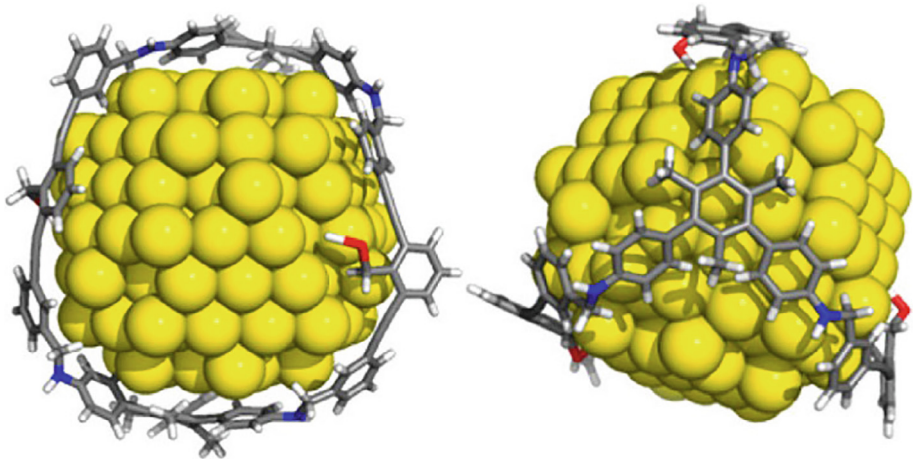

Fig. 13. Simulated lowest energy structure of gold nanoparticles with the radius of 8.65 Å inside cage **17**.[75].

interactions. The energy minimum is achieved in the presence of AuNPs with the radius of 8.65 Å, after which a significant increase in energy is observed for AuNPs having the radius of 9.99 Å. Overall, the experimental and computational results, shown in Fig. 13, are in good agreement, meaning the *in situ* liquid–liquid approach for the templated synthesis of AuNPs is a facile method to preparing other metal NPs in similar discrete molecular cages.

Due to their multielectron accepting nature, fullerenes have potential in various energy conversion and electrochemical applications such as photovoltaic devices, lithium ion batteries and electrocatalysis.[76,77] The arrangement of fullerenes can alter their electrical conductivity and their ordered clustering can lead to superior optoelectronic performance relative to the bulk.[78] Stoddart and co-workers synthesized a cyclophane which binds C_{60} in a 1:1 ratio and forms one-dimensional arrays along the long needle-like single crystal axis.[78] The conductivity of these crystals is 2–3 orders of magnitude higher than that of previously reported undoped C_{60}. The semiconducting nanowires were prepared under ambient conditions and could be used for various electronic devices such as organic field-effect transistors and organic photovoltaic solar cells.

Nanoconfinement can also be used to stabilize naturally unstable and rare species. Endohedral metallofullerenes (EMFs) are a class of fullerenes which contain metal atoms or metal clusters. [79] A review article published in 2008 by Martin and co-workers discusses the chemistry and nano-forms of carbon, along with the isolation and encapsulation of molecules inside endohedral metallofullerenes.[80] Work on EMFs has generally focused on the isolation of unstable materials and lanthanides inside the fullerene cages, but recently the interest has fallen toward actinides due to their richer valence states and electronic structures compared to lanthanides.[79,81] Computational studies have suggested that the encapsulation of actinides inside EMFs can result in unique and unexpected ligand–metal bonds and cage structures. [82] Such systems have potential applications in nuclear medicine.

In 2017, the Chen group reported the first crystal structure of an actinide inside the C_{82} fullerene.[81] The authors successfully prepared a single crystal of C_{82} with a single encapsulated thorium ion. SXRD analysis of the crystal revealed unique behaviour of the metal ion inside the fullerene. More specifically, the thorium ion is centred above a cage carbon atom with a coordination bond length of 2.340(14) Å with three longer (in the range of 2.411(9) to 2.494(10) Å) coordination bonds to the adjacent carbon atoms. This position of the thorium ion is different from its conventional complexes where the metal ion is centred above the cyclopentadiene ring rather than a specific C atom. Importantly, this unique confinement interaction results in strong fluorescence behaviour of the fullerene, which is uncommon for independent, *i.e.* empty and non-encapsulated, fullerene and thorium compounds.

Unsupported non-bridged uranium–carbon double bonds do not commonly appear in nature and require non-standard synthetic conditions.[83] Furthermore, these compounds are difficult to isolate. For instance, the isolation of non-chelated U = C species has been achieved only on rare occasions by using methanediide or ylidic ligands.[84,85] In 2018, the Chen group reported the first crystal structure of a diuranium carbide cluster, U = C = U, inside a C_{80} fullerene cage.[83] SXRD analysis revealed a carbide-bridged structure in which the uranium–carbon bond lengths are the shortest reported among poly-coordinated uranium complexes (2.03 Å). Confinement of this U = C = U cluster results in the first ever reported unsupported U = C bonds.

Following this work, Chen and co-workers reported in 2019 the first crystal structure of isolated U_2C_2 clusters inside fullerenes C_{78} (U_2C_2@C_{78}) and C_{80} (U_2C_2@C_{80}).[86] The U–C bond lengths vary from 2.130 to 2.421 Å, indicative of single bonds unlike in the case of the U = C = U cluster. The difference in confinement environments (C_{78} and C_{80}) resulted in U_2C_2 clusters adopting different bond lengths and angles. The U–U distance for U_2C_2@C_{78} of 4.164 Å is longer than that of U_2C_2@C_{80} which is 3.855 Å. The authors highlight that the fullerene cages impose steric effects, which lead to both clusters adopting a "butterfly" shape while U_2C_2 clusters by themselves prefer the planar geometry.

In 2022, Feng and co-workers reported on a Ho_2C_2 cluster with two configurations inside a $C_2(61)$-C_{92} fullerene cage.[87] The authors prepared holmium-encapsulated fullerene cages *via* the arc-discharge method and isolated two isomers of the EMFs using high performance liquid chromatography. Single crystals of Ho_2C_2 inside the fullerene cage were prepared by slow evaporation of the EMFs with Ni^{II}(OEP)_in toluene. SXRD analysis reveals that the guest metal cluster exhibits flexible configurations inside $C_2(61)$-C_{92}. Due to the high symmetry of the structure, the holmium sites are disordered inside the cage and were first refined freely and then paired. This results in two pairs of holmium sites (Ho1D with Ho2D and Ho1A with Ho2A). The Ho1D—C—C—Ho2D pair exhibits a planar zigzag configuration inside the EMF while the Ho1A—C—C—Ho2A exhibits a folded butterfly-like configuration. DFT calculations at the B3LYP/6-31G*∼SDD level both support the presence of both conformers with a small difference in distortion energy (1.371 kcal mol^{-1}), suggesting that the metal cluster is likely to be flexible over the determined range. Cyclic voltammetry shows different redox potentials for both isomers with electrochemical band gaps of 1.24 and 1.35 V.

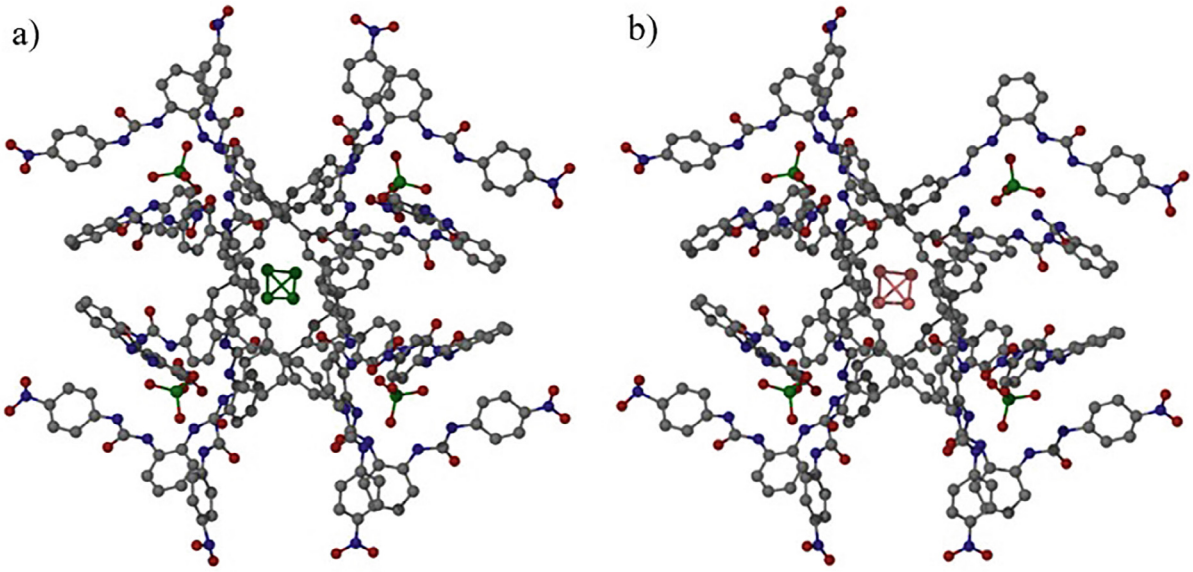

Fig. 14. Single crystal structures of tetrahedral a) white phosphorus inside the cage of **18** and b) yellow arsenic inside the cage of **18**. Gray: C. Red: O. Blue: N. Green: P. Purple: As. Hydrogen atoms have been omitted for clarity.[91].

The magnetic properties of metallosupramolecular cages can be tuned by exchanging various guest molecules inside their voids. Brechin and co-workers prepared a tetrahedral M_4L_6 metallosupramolecular cage with quaterpyridine (**L**) and nickel, which form $Ni^{II}_4\mathbf{L}_6$ cages, to study the effect of the encapsulation of paramagnetic MX_4 guests on the magnetic properties of the host.[88] Crystal structures of host–guest complexes were prepared *via* vapour diffusion of the guests $M^{II}X_4$ ($MnCl_4^{2-}$, $CoCl_4^{2-}$, $CoBr_4^{2-}$, $NiCl_4^{2-}$ and $CuBr_4^{2-}$) or $M^{III}X_4$ ($FeCl_4^{3-}$ and $FeBr_4^{3-}$) in THF into $Ni(OTf)_2$ and **L** in MeCN. The crystal structures of metal halides in $Ni^{II}_4\mathbf{L}_6$ are structurally similar, forming a 1:1 host–guest complex with the cage. DFT calculations show that $[NiCl_4]^{2-}$ exhibits a slight structural deformation upon encapsulation with an estimated distortion energy of 18.6 kJ mol^{-1}. This host–guest pair exhibits unique magnetic anisotropy, wherein the decrease of temperature results in the fastest drop of magnetic susceptibility product. Overall, the authors conclude that these results pave the way towards the potential design and production of unique single-ion magnets with dia/paramagnetic cages having applications in sensing, switching and stabilisation of various species.

3.2. Organic clusters and solid-state clusters of gases

Other naturally unstable species include white phosphorus (P_4) and yellow arsenic (As_4). P_4 is widely used to synthesise organophosphorus materials, but it is highly toxic and pyrophoric while As_4 is the most unstable allotrope of arsenic and converts to gray arsenic under ambient conditions.[89,90] Wu and co-workers synthesised an anionic tetrahedral cage **18** to separate and stabilise P_4 and As_4 inside the cage void.[91] By slowly diffusing diethyl ether into a solution containing freshly sublimed P_4 and **18**, SXRD-quality crystals of P_4 encapsulated cluster inside **18** (**18** ▫ P_4) were obtained in several weeks. For **18** ▫ As_4, an *in situ* approach was taken to dissolve As_4 inside a solution of **18**, followed by similar workup to obtain single crystals of **18** ▫ As_4. Fig. 14 shows the single crystal structures of **18** ▫ P_4 (Fig. 14a) and **18** ▫ As_4 (Fig. 14b). Both encapsulated P_4 and As_4 exhibit parallel configuration to that of the cage, *i.e.* the atoms of the encapsulated guests point toward the vertices of the cage. As computational analysis suggests, this configuration exhibits the most stable orbital interactions between bent "banana" bonds of P_4 and As_4 and π orbitals of cage ligands. It is evident that P_4 is more stable inside the cage void as the average P—P bond length is 2.097 Å, significantly shorter than the previously reported 2.19 and 2.16 Å inside cages by Nitschke and co-workers and Scheer and co-workers, respectively.[90,92] Shortened bond lengths were also found for the case As_4 inside **18** compared to the bond lengths reported by Scheer and co-workers.[90] Capture and release capabilities of the cage were tested by introducing tetramethylammonium cations (TMA^+) to a mixture of deuterated acetonitrile (CD_3CN) and **18** ▫ P_4 and monitoring the changes on the ^1H and ^{31}P NMR spectra. Upon the addition of TMA^+ to CD_3CN, the signals corresponding to free P_4 increased while those of encapsulated P_4 decreased, indicating a release of P_4 from the cage void.

In 2017, Nitschke and co-workers reported host–guest complexes between C_{60} and a porphyrin-edged metal–organic polyhedron.[93] The complexes are synthesised by reacting polyhedron tetrafluoroborate salts with excess C_{60} for 24 h at 298 K. Depending on the solvent, up to four C_{60} molecules entered each polyhedron pore, with each host–guest system exhibiting different electronic behaviour. Single crystals of the cages with one and three encapsulated C_{60} molecules were obtained and their single crystal structures are shown in Fig. 15. In the case of three guests, C_{60} molecules occupy-three faces of the polyhedron, leaving one empty. Nitschke and co-workers suggest that this arrangement is favoured due to host–guest and guest–guest π–π stacking interactions. This is supported by the placement of one C_{60} guest inside the pores which was located by one face of the polyhedron. Thus, the positioning of the three C_{60} guests is most likely a result of stabilizing π–π interactions rather than steric effects. Crucially, the electron affinity of the systems with multiple C_{60} guest molecules is higher than that of pure polyhedra and one encapsulated fullerene, implying potential applications in electron transfer applications.

Similarly to MOFs, cages can be used to capture and release environmentally unfriendly gases. One of those gases is sulfur hexafluoride, which has been produced since 1953 primarily for insulation of electrical equipment and degassing of molten aluminium

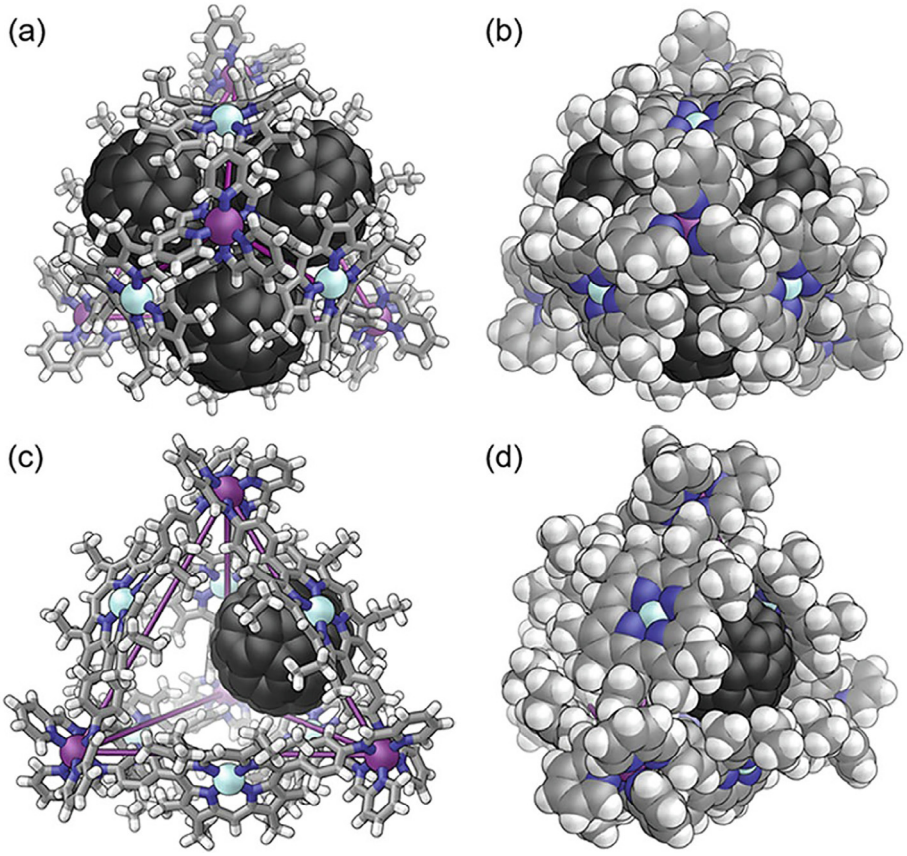

Fig. 15. Crystal structures of three (a and b) and one (c and d) fullerenes encapsulated inside the polyhedra. White: H. Gray: C. Cyan: Ni. Purple: Fe. Blue: N. Black: C_{60}.[93].

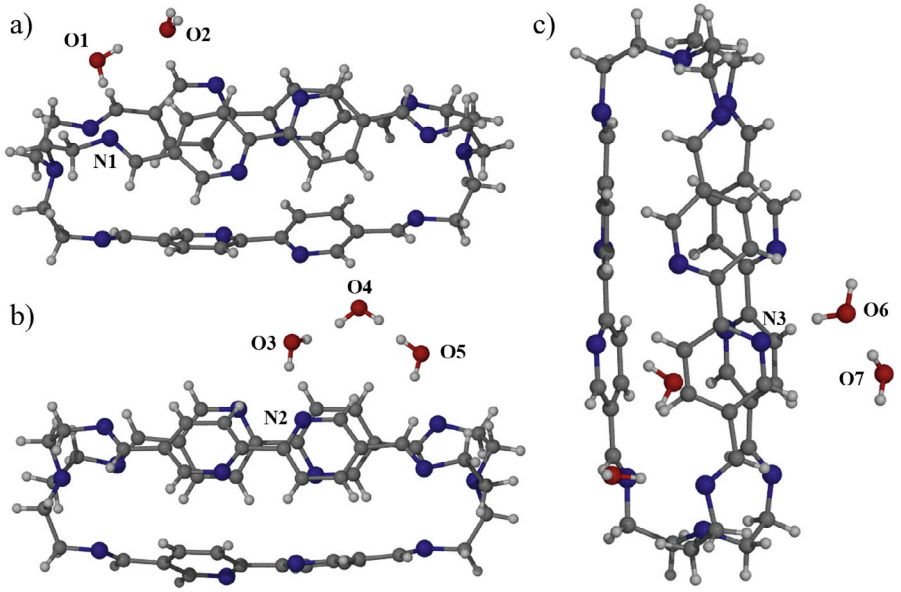

Fig. 16. Single crystal structures of a) $2H_2O$@BPy-Cage, b) $3H_2O$@BPy-Cage and c) $4H_2O$@BPy-Cage. Gray: C. Red: O. Blue: N. White: H.[102].

or magnesium.[94] SF_6 has been acknowledged as a greenhouse gas in the Kyoto protocol. Its negative impact comes from its highly efficient absorbance of infrared light, coupled with an atmospheric lifetime of 3200 years resulting in a global warming potential (GWP) value of 23 500 (for comparison, GWP for CO_2 is 1).[95] In 2011, Nitschke and co-workers synthesised a tetrahedral cage **19** to capture, store and release SF_6.[96] SF_6 gas was bubbled through a solution of deuterated water containing **19** and left in an

environment of SF_6 for three hours, after which ^1H and ^{19}F NMR spectra of the material was obtained. ^{19}F NMR spectra reveal a downfield shift of the signal corresponding to free SF_6 indicating that the target guest is encapsulated inside **19** (**19** ▫ SF_6) with a maximum of 75 % of cages occupied by SF_6. Single crystals of **19** ▫ SF_6 can be obtained by diffusing1,4-dioxane into a water solution of **19** ▫ SF_6. SXRD analysis of **19** ▫ SF_6 reveals that the guest occupies 53 % of the void volume (in close agreement with Rebek's rule[97]) and can be loaded into a saturated solution of **19** at a concentration of 6.6 mM, an increase of 30 times compared to solubility of pure bulk SF_6 in water. In 2014, Nitschke and co-workers also reported on the selective encapsulation of PF_6 inside a mixture containing different cages.[98].

Nuclear energy is a clean and low-carbon energy source, making it an attractive energy source to fight against climate change. Additionally, because of their high demand, fossil fuels are expected to run out within the next 153 years at current demands, while nuclear energy could sustain the planet's energy need for thousands of years.[99] However, radioactive iodine isotopes ^{129}I and ^{131}I pose serious effects on the environment if released as a result of nuclear energy production.[100,101] Chi and co-workers synthesized a bipyridine-based nonporous adaptive cage (BPy-Cage) capable of iodine adsorption from vapour and dissolved in organic solvents.[102] Crystallization of the cage yields three different crystals of the cage hydrate containing two, three and four water molecules ($2H_2O$@BPy-Cage, $3H_2O$@BPy-Cage and $4H_2O$@BPy-Cage, respectively in Fig. 16a, b and c) in the asymmetric unit. In $2H_2O$@BPy-Cage, the O1···N1 hydrogen bond length is 2.91 Å and the O1···O2 hydrogen bond is 2.76 Å, indicative of a strong hydrogen bond. In $3H_2O$@BPy-Cage, three water molecules form a trimer. The O3···N2 hydrogen bond distance is 2.86 Å and the O3···O4 and O4···O5 distances are 2.83 and 2.75 Å, respectively. In $4H_2O$@BPy-Cage, the O6···N3 and O6···O7 distances are 2.83 and 2.87 Å, respectively. These results indicate that the first water molecule is likely to form a hydrogen bond with a nitrogen atom of the cage and acts as a seed where further water molecules can nucleate *via* hydrogen bonding. The dimers and trimers shown in Fig. 16 a and b both exhibit shorter hydrogen bonding distances for water–water interactions compared to water–cage. Thus, the addition of the second and third water molecules could have a stabilising effect on the water cluster and can promote the adsorption of water molecules. The authors state that the origin of water molecules in the crystal structures is from trace water in the crystallization solvents. Crucially, this shows selective adsorption of water to the adaptive cage system and water adsorption and potentially cluster evolution could be studied using SXRD.

Iodine vapor adsorption of Bpy-Cage reaches up to 3.23 g g^{-1}, increasing in a linear fashion and corresponding to 21 iodine molecules per cage. Upon immersion in DMF, Bpy-Cage releases the adsorbed iodine and after desolvation can adsorb iodine as effectively as the as-synthesized material. Crucially, considering the linear uptake along with the high crystallinity of this cage, evolution of I_2 uptake could be potentially studied using SXRD, revealing the mechanism of adsorption and the resulting conformational changes of the adaptive cage. This would shed light onto future adsorbent design for efficient and selective I_2 sorption applications.

Chiral luminescent materials have a myriad of potential applications in catalysis, sensing and the security sector.[103–105] However, host–guest chemistry with luminescent and chiral materials is a relatively unexplored field. Sun and co-workers recently prepared the first lanthanide-based tetrahedral cage which exhibits guest-driven self-assembly and chiral induction.[106] Treating 1.0 equiv. of ligand with 1-pyrenecarboxaldehyde (1-PCA, 0.75 equiv.) and $Eu(OTf)_3$ (1.1 equiv.) results in the formation of the tetrahedral cage **20** with a dynamic radius of 1.77 nm. After the removal 1-PCA from the cage void, the Eu_4L_4 cage transforms into Eu_3L_3 within 12 h, so guest-driven transformation back to Eu_4L_4 was performed with a range of polyaromatic molecules. Full transformation is achieved with 1-pyrenecarboxaldehyde at 3 equiv. while 80 equiv. of benzothiophene is required to achieve the same result. Crystal structures of all seven polyaromatic guests inside cage **20** were obtained *via* the slow evaporation method. Three 1-PCA molecules were located inside **20** along with many other guests while four phenanthrene, benzothiophene and naphthalene were encapsulated inside **20**. In the case of three encapsulated guests, the guests are aligned parallel with the triphenyltriazine ligand forming π–π interactions along with additional weaker C—H···π guest–guest interactions. Thus, significant changes in the packing modes of the guests are observed compared to their bulk packing arrangements. For instance, bulk pyrene exhibits displaced parallel π–π interactions while encapsulated pyrene molecules form a C_3 spin arrangement preventing the formation of excimers. By mixing pyrene-encapsulated Eu_4L_4 and Tb_4L_4 cages, the authors successfully prepared a white-light emissive sample.

Overall, the ability to study encapsulated guest molecules under nanoconfinement using SXRD reveals potential binding mechanisms, stacking arrangement and the effect that the size and shape of both host and guest materials have on the nanoscale molecular recognition of these systems. This is valuable information for future design of porous materials which utilise the nanoscale conformation of molecules to tune their physicochemical properties for desired applications. Tuning the window sizes of porous compounds (*i.e.* cages, MOFs and metal organic polyhedra) can also be used to selectively keep out solvent molecules in order to encapsulate smaller guests. In this sense, confinement is introduced into a liquid by dissolving or mixing porous materials so that the solvent is sterically too big to enter the cavities of the porous materials, thus making a porous liquid (PL). Types 1, 2 and 3 PLs have been reported, and a recent review article by Gascon and co-workers was published in 2019.[107] From the aspect of crystallization under nanoconfinement, PLs could pose a very interesting concept. If confining matrices could be used to selectively crystallize a desired polymorph under nanoconfinement in solution, then potentially applying external stimuli to disassemble the matrix and grow the polymorph in bulk could be feasible. This method could be highly desired in the pharmaceutical industry, for example.

4. Crystallization under confinement

This section will provide a discussion of how confinement affects various aspects of crystallization such as nucleation and crystal growth processes, freezing and melting point depression and polymorphic and morphological control. In 1998, Luzzi and co-workers prepared ordered C_{60} inside carbon nanotubes.[108] The authors used pulsed laser vaporization of graphite in the presence of metal catalysts, followed by HRTEM imaging of the as-prepared material. The images show an ordered array of C_{60} cages inside the nanotube with the fullerene centre-to-centre distances of 1.0 nm. While in this case C_{60} does not necessarily crystallize inside the nanotubes, it is an example of molecules forming an ordered structure under nanoconfinement. Ultimately gaining control of molecular ordering processes under nanoscale is a powerful tool toward crystallization of desired materials and their polymorphs. An extensive review article on crystallization under confinement by O'Shaugnessy and Meldrum published in 2020 is highly recommended for an interested reader.[109] The authors review the effect that various confining matrices with different shapes and sizes have on crystallization processes, freezing and melting points. As this section is not meant to be as exhaustive as the work by O'Shaugnessy and Meldrum, we will briefly discuss

what we believe are important findings in the field of confinement crystallization, followed by relevant work published since the 2020 review.

4.1. Crystallization in nanopores

In 2000, Green and co-workers reported on the crystallographic analysis of one-dimensional single crystals of potassium iodide grown inside 1.6 nm single-walled carbon nanotubes (SWCNTs).[18] Crystals grown in the SWCNTs are merely-two or three atoms wide but extend to tens of micrometres in length. Using HRTEM imaging, single atoms of potassium or iodide can be resolved and the crystal packing analysed. The packing arrangement of KI inside the nanotubes is different from that of bulk KI. In bulk, the lattice coordination is 6:6 while in the nanotube the face and edge atoms have 5:5 and 4:4 coordination, respectively. In addition, the crystals contract along the *c* axis as compared to the bulk, from K–I distances of 0.705 in bulk to 0.695 nm inside the nanotubes. Apart from the 1.6 nm nanotube, the KI was also crystallized inside nanotubes with different diameters. Crucially, the authors note that selective crystallization of desired strain states of KI crystals can be achieved by tuning the nanotube diameter.

In a 2005 review, Alcoutlabi and McKenna showed that the glass transition temperature of materials can change as a result of their confinement in nanopores.[15] Although a conclusive explanation to this phenomenon was not given, the authors hypothesised that this change in thermal properties of materials could be due to the intrinsic size effect, sample preparation, confinement effects, or a combination of thereof. Still, the results reviewed by Alcoutlabi and McKenna could be still interpreted as a result of confinement effect, which begs the question of whether confinement could also affect the processes of nucleation and/or crystallization. In fact, substantial evidence exists to support the hypothesis that confinement affects these crystallization processes. For instance, confinement effects on crystallization are observed when form I of anthranilic acid (AA) is heated to 155 °C and subsequently cooled down to room temperature inside the confined space of controlled pore glass (CPG) with diameters of 55, 23 and 7.5 nm.[19] The cooling step results in the formation of different polymorphs within CPGs of varying diameters. Inside CPG with a diameter of 55 nm, only form III is revealed by PXRD. The metastable form II of AA forms partially within the CPG of 23 nm in diameter while it is found in abundance inside the smaller CPG with 7.5 nm diameter. The formation of form II is attributed to the smaller critical nucleus size compared to those of form I and III.

Crystallization under confinement has also led to the discovery of size-dependent polymorphism, a phenomenon in which different polymorphs form depending on crystal size. Ward and co-workers performed nanoscale crystallization experiments on select α,ω-dicarboxylic acids and coumarin inside the pores of CPG and porous poly(cyclohexylethylene) (p-PCHE).[17] Recrystallization of bulk β-glutaric acid (β-GA) by cooling its melt produces the polymorph α-GA, which transforms to β-GA within 1 h at room temperature. However, by cooling the melt inside 7.5, 23 and 55 nm CPG results in the crystallization of α-GA nanocrystals, which are stable at room temperature for months without transforming into β-GA. In the case of pimelic acid (PA), a new polymorph, δ-PA, was obtained *via* heating and cooling a methanolic solution of the solvate inside 7.5 nm CPG. Alas, δ-PA slowly transforms into α-PA over the course of a month. However, δ-PA crystallized from the PA melt inside 14 nm p-PCHE is stable for more than a year. A new polymorph of coumarin (C), β-C, was also obtained by crystallization from 23 nm CPG while crystallization from bulk forms the α-C polymorph. Both α-C and β-C forms are obtained inside 7.5 nm CPG and exclusively α-C forms inside 55 nm CPG. Overall, this work illustrates the polymorphic size-dependence upon crystallization where different polymorphs of a compound preferentially form depending on the limitations on the crystal size.

Following this work, Ward and co-workers reported on the preferred orientation of crystals of other α,ω-dicarboxylic acids under nanoscale confinement in p-PCHE pores of 14, 30 and 40 nm in size.[110] Crystals were grown by either imbibing a melt or a methanolic solution of the target compound in the pore walls. Malonic acid (C3) nanocrystals grown inside p-PCHE result in the formation of the α-C3 polymorph. More specifically, the nanocrystals align along the α(0 1 0) and α(0 0 1) planes, perpendicular to the pore wall and pore direction, respectively. For glutaric acid (C5), when nanocrystals are grown using the methanol solution method, the 14 nm pores exclusively exhibit the α-C5 form while in pores of 30 and 40 nm the β-C5 form is found, showing the effect of confinement on polymiorphic outcome. On the other hand, the melt method produces α-C5 nanocrystals inside p-PCHE of 30 and 40 nm. Compared to the α-C5 grown in 14 nm pores, the α-C5 grown in 30 and 40 nm pores exhibit a 90° change in the nanocrystal orientation, ascribed to surface energy effects that become apparent at such length scales. Similarly to C5, pimelic acid (C7) also exhibits size-dependent polymorphism – α-C7 grows inside 14 nm pores while a mixture of α-C7 and δ-C7 (a novel polymorph) grows inside 30 nm and exclusively δ-C7 grows inside 40 nm pores of p-PCHE. Bulk crystals of α-C7 grown in benzene are needle-like with the α[20 $\bar{1}$] long axis while the nanocrystals exhibit the α[0 1 0] long axis along with the α(10 $\bar{3}$) plane aligned perpendicular to the pore direction. The authors suggest that the preferred orientation of C7 stems from critical size effects not solvent effects due to the minimization of the (10 $\bar{3}$) surface. Overall, the authors suggest that the preferred orientation of crystals under confinement is the result of critical size and surface energy of nuclei. The results indicate that precritical nuclei that are aligned with their fast growth axis along the pore direction are more likely to reach the critical size due to the minimization of the higher surface area planes. This can result in the formation of crystals in unique orientations and vastly different from those grown in bulk. Along with the reported size-dependent polymorphism, crystallization under confinement can result in unique material physical and chemical properties.

In 2013, the Ward group reported on crystallization of glycine inside anodic aluminium oxide (AAO) ranging from 20 to 2000 nm in pore diameter.[111] Inside the pores of AAO, β-form crystallizes initially and is stable indefinitely ααat ambient temperatures. However, when RH is increased to 90 % for 24 h, the crystals transform to the α-form as revealed by two-dimensional μ-XRD. The addition of a droplet of water results in defects in the crystal structure of β-glycine, which triggers the solid-state transition to α-glycine. To further study the solid-state transition mechanism, the effect of chiral amino acids was examined. Interestingly, most racemic amino acids suppress the transition to the α form, potentially due to the amino acids binding to the {0 1 0} faces of the crystal structures and forcing the crystals to grow in the [0 0 1] rather than [0 1 0] direction. When enantiopure amino acids are added to the AAO pores prior to crystallization, β-glycine crystallizes in the [0 1 0] direction and transforms into α-glycine after the RH is increased. Overall, the authors are able to demonstrate the suppression of a polymorph transition under nanoscale confinement by binding racemic amino acids to the polar {0 1 0} faces of β-glycine.

Apart from mechanistic insights into crystallization, physical properties such as pressure of a growing crystal can also be studied

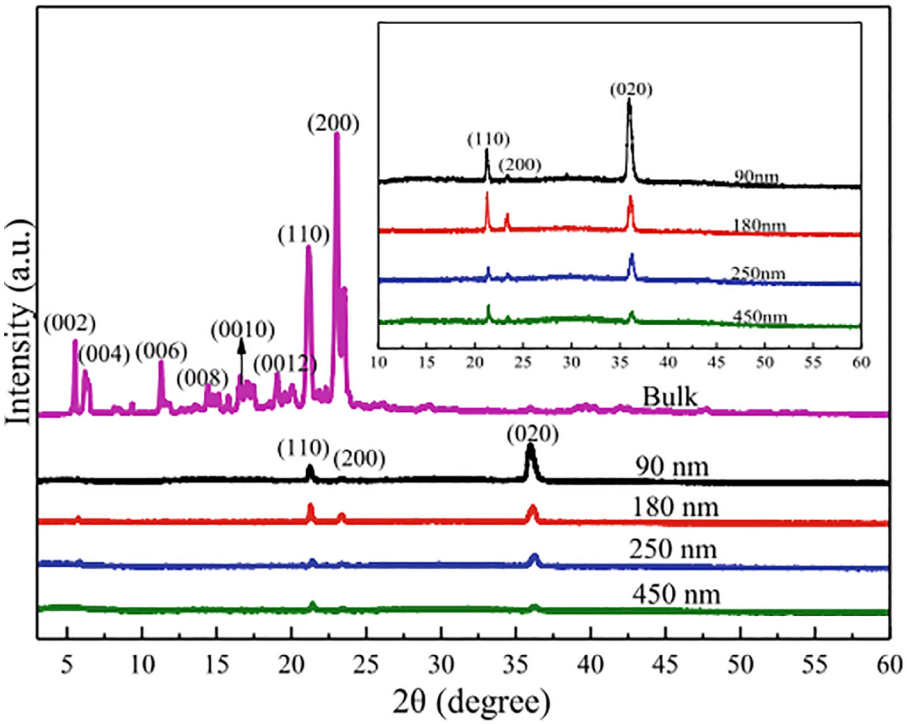

Fig. 17. WAXD diffraction patterns of bulk and AAO-confined PDP. Reproduced from ref. 102 with permission. Further permissions relating to this publication should be directed to ACS. The work can be obtained from: https://pubs.acs.org/doi/10.1021/acsomega.1c02112.

under confinement. Desarnaud *et al.* studied the force exerted by alkali halide, sodium chloride (NaCl) and potassium chloride (KCl), crystals during crystal growth between hydrophilic and hydrophobic glass walls at the nanoscale.[112] The authors use a custom setup in which they are able to control the distance between the glass slides and measure the force exerted on the plate during crystal growth. When crystallization occurs between hydrophilic glass slides, the measured pressure is 220 ± 50 MPa, which is strong enough to damage sandstone. Crystallization between hydrophobic glass slides results in the crystal growing between the slides without the formation of a thin film between the crystal face and the glass slide and thus no pressure is measured. The pressure arises from a repulsive force between the negatively charged crystal face and glass surface, which is separated by the thin film. The presence of the thin film between the crystal face and glass slide is crucial as it allows for more ions to be added to the crystal resulting in further growth and pressure exerted.

Linear chain alkanes can be used as model compounds to study the crystallization processes of polymers as the former are the building blocks of polymers. In addition, crystallization properties of *n*-alkanes are easier to study while polymers exhibit complicated crystallization processes.[113] Crystallization of 3-pentadecylphenol (PDP) as the model compound with the phenol end group was recently studied by Luo and co-workers to gain insight into the crystallization processes and thermal behaviour of polymers that have similar end groups.[114] PDP was confined within the 90, 180, 250 and 450 nm pores of AAO (AAO-PDP) *via* the melt infiltration method and crystallized by cooling from 60 °C to 0 °C. Wide-angle X-ray diffraction reveals that AAO-PDP exhibits two different crystallographic space groups *Pbcm* and *Fmmm* while bulk PDP crystallizes in the *Fmmm* space group. The diffraction peaks corresponding to the *Pbcm* space group become more distinct in the diffraction pattern with decreasing pore size of AAO (Fig. 17). This solid–solid phase transition is thus more pronounced at smaller confined spaces. In addition, the crystallinity of AAO-PDP decreases with decreasing pore radii, which was also found to be true during crystallization of the linear analogue *n*-pentadecane (C_{15}). However, the decrease in crystallinity is more pronounced for AAO-PDP samples indicating that the presence of the phenol end groups disturbs crystallization under confinement more than linear alkyl chains. This suggests that introducing different end groups to small organic molecules and polymers can result in different crystallization processes, which can be eventually used to adjust the confined crystallization behaviour of semicrystalline and polymer compounds.

Deep eutectic solvents (DESs) are a class of solvents that offer a "greener" alternative to common solvents due to their low vapour pressure which means they do not evaporate into the environment as readily.[115] In addition, DESs can be designed to biodegradable at low costs. The physical, chemical and thermal properties of DESs have been widely studied, but it was only recently when Lan *et al.* studied the thermal properties and cold crystallization of a DES, reline, under confinement for the first time inside CPG.[116] Reline exhibits melting point depression when confined inside the 50, 100 and 300 nm pores of CPG. In addition, the cold crystallization temperature increases under confinement compared to bulk reline. XRD patterns of bulk reline and confined reline crystals inside 100 and 300 nm CPG pores show similar reflections at 21.6°, 25°, 33.1° and 33.5°. However, an additional peak at 20.5° is present in the confined crystals. As no crystal structure of reline is known, the reflection could not be indexed and thus it is unknown what this peak represents. On the other hand, reline crystallized in 50 nm pores exhibits a different XRD pattern which does not correspond to neither reline nor to the individual components (choline chloride and urea). The authors conclude that this pattern most likely corresponds to a new crystal structure of reline.

Imidacloprid (IMI) is the most widely used insecticide to control the *Aedes* mosquito, and potentially the *Anopheles* and *Culex* mosquitoes.[117,118] However, the usage of IMI has resulted in soil, surface and underwater contamination, along with the decline of

bee colonies. Thus, if the lethality of the insecticide could be increased, then the subsequent decrease in its required concentration would have a positive impact on the environment. Recently, seven new polymorphs (forms III–IX) of IMI, on top of the two previously known forms (forms I and II), were reported by Kahr and co-workers.[118] Of those seven forms, one (form VII) was obtained by nanoconfined crystallization. More specifically, form VII was obtained by crystallizing from a melt in CPG of pore sizes 35, 100 and 200 nm. This form was not characterised by SXRD analysis due to rapid cross-nucleation of form II when seeding larger crystals of form VII in bulk. Lethality studies showed that form IX ranks as the fastest acting insecticide towards female fruit flies and mosquitoes. The lethality ranking matched identically the metastability chart, *i.e.* the more thermodynamically stable the polymorph, the less lethal it is. Form VII ranks as the third least stable form, thus indicating it could be an effective insecticide. Overall, these results indicate the potential of confinement chemistry to increase the efficiency of materials by uncovering novel polymorphs.

Another highly polymorphic compound is flufenamic acid (FFA), an API used for the treatment of various inflammatory conditions. To date, nine polymorphs (forms I-IX) are known, with the first polymorph discovered as early as 1973.[119–121] Conventional bulk crystallization of FFA results in the formation of form I. Ward and co-workers used CPG with pores ranging from 4 to 200 nm to study polymorphic phase transformation under nanoscale confinement.[122] Under confinement of 4 and 8 nm CPG, amorphous FFA forms and remains stable for at least 6 months. However, under 30–200 nm confinement for VIII crystallizes first, confirmed by PXRD analysis. The results indicate that the polymorphic transitions can be dictated by varying the confinement imposed by CPG. For instance, form VIII forms first in CPG pores of 30–50 nm and transformation into forms II and I + II occurs over the course of 3 days and 6 months, respectively. However, in CPG pores of 100–200 nm, form VIII transforms into form IV and IV + III within 20 min and 3 days, respectively. Finally, in bulk, form VIII converts directly to form III upon heating. The authors conclude that nanoconfinement, on top of altering polymorph stability rankings, can also reshape polymorphic transformation pathways and unveil otherwise hidden pathways.

4.2. Crystallization in droplets

Crystallization within microemulsions poses another method to confine the crystal growth of a compound and study the crystallization processes on a nanoscale.[123] Generally, a mixed solvent system containing a surfactant, solvent and the target compound is prepared, which is then either shaken or sonicated to obtain microemulsions that contain the target compound. The constituents can be mixed at elevated temperatures to obtain high saturation of the target compound, and the resulting mixture is then cooled to induce crystallization. In 2007, water crystallization from microemulsions was used to directly measure the critical nucleus size of ice molecules as water freezes.[124] For water pool with radii 1.2–1.8 nm, the critical nucleus contains between 90 and 350 molecules as determined by small-angle X-ray scattering (SAXS).

Microemulsion crystallization has also been used to obtain nanocrystals of mefenamic acid and 5-methyl-2-[(2-nitrophenyl) amino]-3-thiophenecarbonitrile (ROY).[123] For mefenamic acid, a concentration-dependent crystallization of the two known forms of the compound is observed. At lower supersaturations, predominantly the most stable form I is obtained while at higher supersaturations, the metastable form II becomes increasingly predominant. Glycine was also crystallized by adding methanol microemulsions to an aqueous glycine microemulsions to induce crystallization due to the lower solubility of glycine in methanol compared to water. Three polymorphs of glycine (α, β and γ forms) are known out of which γ-glycine is the most stable. The authors note that the most stable form is difficult to obtain from aqueous bulk solutions without the addition of additives or at very low supersaturation. Attenuated total reflectance-Fourier transform infrared (ATR-FTIR) was used to characterise the crystals that appeared after three weeks. At higher glycine concentrations, α-form is predominant and almost exclusively crystallized while at lower supersaturation concentrations, the γ-form becomes predominant. Bulk crystallization of neither glycine nor mefenamic acid do not yield the most stable form due to high nucleation barriers, which are overcome through three-dimensional nanoconfinement in microemulsions. Under confinement, thermodynamic control, *i.e.* crystallization of the most stable polymorph, is achieved by using low supersaturations which favour the crystallization of the most stable forms of glycine and mefenamic acid. Overall, the authors show that it is possible to attain thermodynamic control in nanoconfined systems. This is achieved by first finding the environment in which molecules are stabilized solely by nanoconfinement and subsequently increasing the supersaturation inside the confined systems until thermodynamic control is reached, *i.e.* until the energy barrier to form stable nuclei of the most stable form is overcome.

In 2020, Hao and co-workers found that it is possible to control the morphological outcome of crystallization in microemulsions by varying the water-to-surfactant molar ratio.[125] Previous reports show that higher initial supersaturation upon crystallization from microemulsions leads to the formation of α-glycine while γ-glycine predominantly forms at lower supersaturation.[123,126] The Hao group used a nonionic surfactant in combination of different molar ratios of water to control the morphological and polymorphic outcome of glycine crystals. Antisolvent and cooling microemulsion crystallization were performed within microemulsions ranging from 1 to 5 nm as determined by SAXS. During antisolvent crystallization, polyhedral and needle-like crystals of glycine formed at high and low supersaturations, respectively. At high supersaturation, the microemulsion droplet can be imagined to be crowded by glycine molecules and rapid nucleation results in the glycine clusters agglomerating in different orientations, thus forming polyhedral crystals. In the case of lower supersaturation, the nucleation process is slowed down and oriented attachment of glycine clusters takes place resulting in needle-shaped crystals. Accordingly, both needle-shaped and polyhedral crystals of glycine are obtained under medium supersaturation. Interestingly, both needle-like and polyhedral crystals are those of α-glycine polymorph. This is due to the hydrophilic poly(oxyethylene) groups of the surfactant orienting in a winding shape when dissolved in water, which promotes the growth of α-glycine.

The pharmaceutical industry relies heavily on batch crystallization to consistently produce the desired polymorphs of small molecule active pharmaceutical ingredients (APIs). However, inconsistent particle size distribution (PSD) of crystals obtained *via* batch crystallization affects manufacturing processes and bioavailability of the APIs.[127] In 2020, Lakerveld and co-workers employed the emulsion crystallization method to control the crystal size distribution (CSD) of ibuprofen.[128] Ibuprofen was selected as it is a widely studied drug and it belongs in class II of the Biopharmaceutical Classification System, where many newly developed drugs also belong.[129] The authors prepared ibuprofen–water–heptane emulsions with various surfactants and crystallized ibuprofen by cooling. The most stable emulsions are formed with the nonionic surfactant Tween 20 while anionic and cationic surfactants are less stable. Using a homogenizer, small droplets form within the emulsion inside which crystallization is expected to occur. However, crystallization from these small dro-

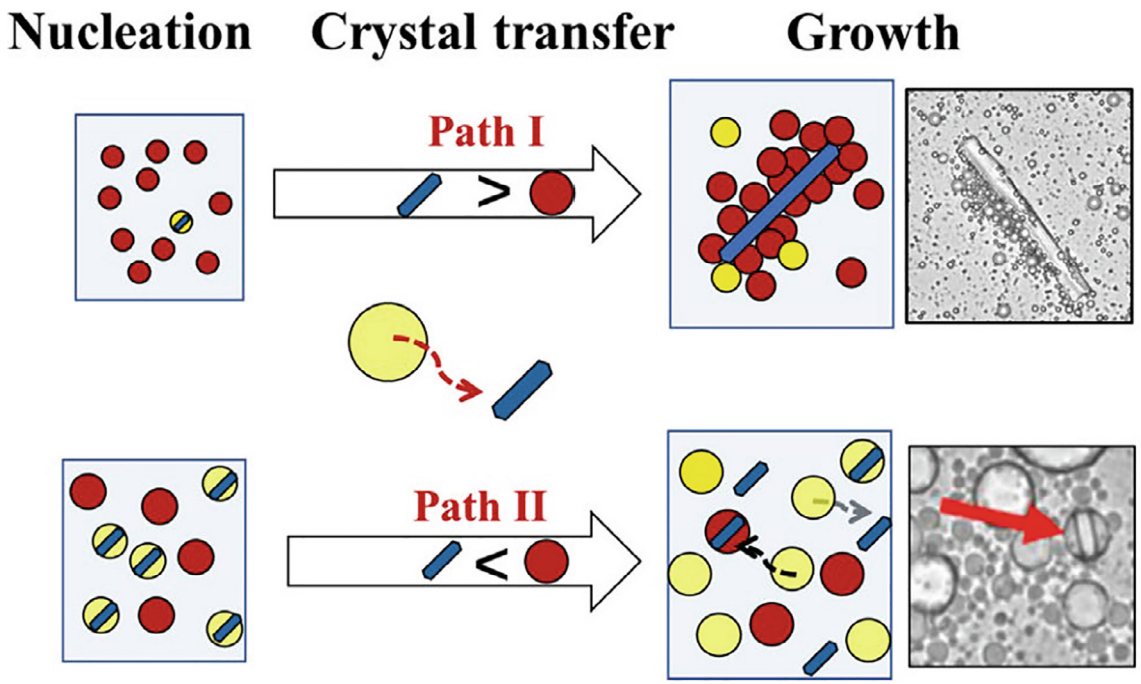

Fig. 18. Illustration of the crystallization pathway in emulsions containing smaller and larger crystals.[128].

plets results in the formation of large crystals due to the droplets attaching together as illustrated in Fig. 18. Thus, crystallization in larger droplets obtained by stirring was undertaken. Larger droplets are able to confine the crystal growth of ibuprofen due to shorter induction time in a macroemulsion, leading to a smaller crystal mean size. Overall, different emulsification methods which result in varying droplet sizes could be a method to obtain consistently small crystals of APIs.

Also in 2020, Lai and co-workers demonstrated two methods of seeded microfluidic crystallization in water–oil emulsions to control the polymorphism and PSD of a small molecule API, abacavir hemisulfate (AH).[130] The first method is that of solvent extraction in a mixed solvent emulsion system, in which a mixture of surfactant in pentyl acetate and API in water solutions are ran through a droplet generator into a petri dish, resulting in a solution in which droplets containing the API are formed in a solution of pentyl acetate. The crystallization of AH is induced by cooling this mixture, which results in spherical agglomerates of the API crystallizing in the droplets. The second method involves combining a seed suspension and dissolved solution of AH, which is then emulsified. The resulting droplets are cooled below the saturation limit to induce crystallization. This method results in successful crystallization of single crystals of AH. In addition, decreasing the concentration of seeds in the input stream results in larger single crystals with an overall decrease in PSD. The authors also demonstrate a novel temperature cycling method to decrease the number of seeds in droplets with the goal to obtain a single seed in every droplet. The cycling process reduces the number of seed crystals from 9 to 3 inside a single droplet. Overall, this seeded droplet microfluidic system grants good control of the PSD of single crystals of an API and can also be scaled up and optimised for manufacturing operations and bioavailability.

Microcapsules are used in various industries such as pharmaceutical, cosmetics and agriculture for storage and delivery applications. Their most common form is that of a solid sphere encapsulating a fluid in which the target compound is dissolved. Recently, Bon and co-workers reported on the fabrication of microcapsules from emulsion droplets.[131] The microcapsules are interlocked by needle-like crystals which crystallize during the evaporation of the solvent. Droplets are formed by injecting a solution containing dichloromethane/dodecane/decane-1,10-bis(cyclo hexyl carbamate (DBCC) into a poly(vinyl alcohol) (PVA) phase. Evaporation of dichloromethane triggers the crystallization process and within 10 min, spiky microcapsules form. The adhesive properties of spiky microcapsules are superior to the smooth equivalents and their shape can be controlled when recrystallized in different geometric confinements.

Overall, crystallization under confinement can be effectively used for polymorphic and crystal size control and to unveil novel polymorphic phase transitions. However, while obtaining novel polymorphs for pharmaceutical applications is highly sought after, it is difficult to predict and obtain the desired polymorphs from bulk solutions which would have advantageous physicochemical properties compared to previously known polymorphs. In this light, using confinement on the scale of tens of angstroms to design matrices to obtain nuclei with a specific shape and size can result in gaining control over the molecular packing of the resulting crystal. Cooper and co-workers showed that controlling the supersaturation under nanoconfinement in microemulsion leads to thermodynamic control over crystallization.[123] In addition, Green and co-workers have confinement of KI in SWCNTs leads to a closer packing of KI, which indicates that crystal size and shape can be controlled as well.[18] These findings suggest that control over crystal form, size and shape could be attained *via* careful design of crystallization matrices and conditions. In addition, further insights into nucleation mechanisms, such as those of Yaghi and co-workers[26] and Lu and co-workers[27], will help to understand the effect of confinement on the formation of stable nuclei, their shape and nucleation rates, which are crucial to reach further achievements in the field of confinement chemistry.

5. Conclusions

Confinement has been proven to be a useful method for various purposes – from controlling chemical reactivity to stabilising

unstable species to enhancing specific properties. So far, mainly microporous MOFs have been utilised to study compounds under confinement. One of the many achievements in the field is CSM and as a result, novel crystal structures have been determined. We believe that the future of this field relies on expanding the library of MOFs that can be used for CSM, especially mesoporous MOFs in which larger aggregates or compounds can be studied *via* SXRD. MOFs with different pore environments and topologies can be used to further evaluate the effect of nanoconfinement on the encapsulated materials. An interesting pathway towards discovering novel polymorphs under confinement would be combining the structures of molecular clusters under confinement with crystal structure prediction calculations. In addition, nanoconfinement inside cage-type molecules has been shown to have potential applications in photovoltaics due to the enhances electronic effects such confinement imposes on guest compounds. Furthermore, confinement can have stabilising effects on compounds that are difficult to isolate or stabilise using ambient conditions or standard synthetic techniques.

Crystallization under confinement is still a rapidly developing field which has promising applications in various industries ranging from textile to pharmaceutical as it allows for a more accurate control of pore size distribution, morphology and polymorphism of target compounds. Furthermore, crystallization using microfluidic systems for pharmaceutical applications can be easily scaled up making it easier to use in industrial settings. In order to reach further achievements in the field, certain challenges will need to be overcome. First, studying nucleation on an atomic level must be feasible in order to understand how it is influenced by various external stimuli such as temperature, pH, concentration, solvent effect, size and geometry of the confining matrices *etc.* Currently, only a few examples of this have been recently reported using MOFs as crystalline sponges. Studying nucleation on such a small scale has also been made more feasible thanks to the development of microED, which allows for significantly smaller crystal samples to be studied at very high resulting crystal structure resolutions. Additionally, a larger array of confining matrices need to be studied in order to better understand how to gain control over nucleation and crystallization processes and outcomes. Finally, a convenient method of separating single crystals grown under confinement using solid-state confining matrices must be formulated. If a desired polymorph is grown, for example, in a MOF then being able to separate the crystal and potentially use it as a seed in bulk crystallization for scale-up can be very useful.

In particular, we want to highlight the potential of using confining matrices such as MOFs and cages to gain further knowledge and possibly control over polymorphism of small organic molecules. Designing confining matrices with selective seeding sites of guest molecules which can then be used to direct the nucleation and crystal growth pathways toward novel polymorphs is a very attractive application. In this sense, MOFs and cages are very attractive confining matrices not only because they can be used as crystalline sponges to determine the structures of encapsulated materials but also due to the versatility of the shapes and sizes of their pores.

Data availability

No data was used for the research described in the article.

Declaration of Competing Interest

The authors declare that they have no known competing financial interests or personal relationships that could have appeared to influence the work reported in this paper.

Acknowledgement

This work was supported by the UK Engineering and Physical Sciences Research Council (grant number EP/T518001/1).

References

[1] D. Muñoz-Santiburcio, D. Marx, Chem. Sci. 8 (2017) 3444–3452.
[2] A.B. Grommet, M. Feller, R. Klajn, Nat. Nanotechnol. 15 (2020) 256–271.
[3] H.G. Hansma, Origins Life Evol. Biospheres 44 (2014) 307–311.
[4] P.L. Urban, New J. Chem. 38 (2014) 5135–5141.
[5] W. Reisner, J.N. Pedersen, R.H. Austin, Rep. Prog. Phys. 106601 (2012) 1–34.
[6] Y. Shichida and T. Matsuyama, Philos. Trans. R. Soc., B, 2009, 364, 2881–2895.
[7] B.C. Tripp, K. Smith, J.G. Ferry, J. Biol. Chem. 276 (2001) 48615–48618.
[8] G.A. Ozin, C. Gil, Chem. Rev. 89 (1989) 1749–1764.
[9] R.A. Sheldon, I.W.C.E. Arends, H.E.B. Lempers, Catal. Today 41 (1998) 387–407.
[10] N.E. Levinger, Science 298 (2002) 1722–1723.
[11] J.E. Boyd, A. Briskman, C.M. Sayes, D. Mittleman, V. Colvin, J. Phys. Chem. B 106 (2002) 6346–6353.
[12] M. Wang, Y. Hou, L. Yu, X. Hou, Nano Lett. 20 (2020) 6937–6946.
[13] H.J.G.E. Gardeniers, Anal. Bioanal. Chem. 394 (2009) 385–397.
[14] H.X. Zhou, Arch Biochem. Biophys. 469 (2008) 76–82.
[15] M. Alcoutlabi, G.B. McKenna, J. Phys.: Condens. Matter 17 (2005) R461–R524.
[16] Q. Jiang, M.D. Ward, Chem. Soc. Rev. 43 (2014) 2066–2079.
[17] J.M. Ha, B.D. Hamilton, M.A. Hillmyer, M.D. Ward, Cryst. Growth Des. 9 (2009) 4766–4777.
[18] R.R. Meyer, J. Sloan, R.E. Dunin-Borkowski, A.I. Kirkland, M.C. Novotny, S.R. Bailey, J.L. Hutchison, M.L.H. Green, Science 289 (2000) 1324–1326.
[19] J.M. Ha, J.H. Wolf, M.A. Hillmyer, M.D. Ward, J. Am. Chem. Soc. 126 (2004) 3382–3383.
[20] D. Shi, B.L. Nannenga, M.G. Iadanza, T. Gonen, Elife 2 (2013) 1–17.
[21] L. Chen, H. Chen, R. Luque, Y. Li, Chem. Sci. 5 (2014) 3708–3714.
[22] S.M. Towsif Abtab, D. Alezi, P.M. Bhatt, A. Shkurenko, Y. Belmabkhout, H. Aggarwal, Ł.J. Weseliński, N. Alsadun, U. Samin, M.N. Hedhili, M. Eddaoudi, Chem 4 (2018) 94–105.
[23] X.N. Wang, P. Zhang, A. Kirchon, J.L. Li, W.M. Chen, Y.M. Zhao, B. Li, H.C. Zhou, J. Am. Chem. Soc. 141 (2019) 13654–13663.
[24] M.I. Gonzalez, A.B. Turkiewicz, L.E. Darago, J. Oktawiec, K. Bustillo, F. Grandjean, G.J. Long, J.R. Long, Nature 577 (2020) 64–68.
[25] S. Ciambellotti, C. Pozzi, S. Mangani, P. Turano, Chem. Eur. J. 26 (2020) 5770–5773.
[26] N. Hanikel, X. Pei, S. Chheda, H. Lyu, W. Jeong, J. Sauer, L. Gagliardi, O.M. Yaghi, Science 459 (2021) 454–459.
[27] C. Lu, B. Maity, X. Peng, N. Ito, S. Abe, X. Sheng, T. Ueno, D. Lu, Commun. Chem. 5 (2022) 1.
[28] K. ichi Otake, H. Kitagawa, Small 2006189 (2021) 1–17.
[29] C. Kang, D. Kim, Arch. Pharm. Res. 43 (2020) 110–117.
[30] J. Qian, X. Gao, B. Pan, Environ. Sci. Technol. 54 (2020) 8509–8526.
[31] G. Tabacchi, ChemPhysChem 19 (2018) 1249–1297.
[32] Y. Inokuma, S. Yoshioka, J. Ariyoshi, T. Arai, Y. Hitora, K. Takada, S. Matsunaga, K. Rissanen, M. Fujita, Nature 495 (2013) 461–466.
[33] J. Liu, T.A. Goetjen, Q. Wang, J.G. Knapp, M.C. Wasson, Y. Yang, Z.H. Syed, M. Delferro, J.M. Notestein, O.K. Farha, J.T. Hupp, Chem. Soc. Rev. 51 (2022) 1045–1097.
[34] C.H. Sharp, B.C. Bukowski, H. Li, E.M. Johnson, S. Ilic, A.J. Morris, D. Gersappe, R.Q. Snurr, J.R. Morris, Chem. Soc. Rev. 50 (2021) 11530–11558.
[35] L.M. Cao, J. Zhang, X.F. Zhang, C.T. He, Chem. Sci. 13 (2022) 1569–1593.
[36] M. Zhang, M.Y. Efremov, F. Schiettekatte, E.A. Olson, A.T. Kwan, S.L. Lai, T. Wisleder, J.E. Greene, L.H. Allen, Phys. Rev. B Condens. Matter Mater. Phys. 62 (2000) 10548–10557.
[37] B. An, J. Zhang, K. Cheng, P. Ji, C. Wang, W. Lin, J. Am. Chem. Soc. 139 (2017) 3834–3840.
[38] F.R. Fortea-Pérez, M. Mon, J. Ferrando-Soria, M. Boronat, A. Leyva-Pérez, A. Corma, J.M. Herrera, D. Osadchii, J. Gascon, D. Armentano, E. Pardo, Nat. Mater. 16 (2017) 760–766.
[39] A.J. Anciaux, A. Demonceau, A.F. Noels, A.J. Hubert, R. Warin, P. Teyssié, J. Org. Chem. 46 (1981) 873–876.
[40] A. Bijelic, M. Aureliano, A. Rompel, Angew. Chem. Int. Ed. 58 (2019) 2980–2999.
[41] M. Samaniyan, M. Mirzaei, R. Khajavian, H. Eshtiagh-Hosseini, C. Streb, ACS Catal. 9 (2019) 10174–10191.
[42] Y. Lu, C. Yue, B. Liu, M. Zhang, Y. Li, W. Yang, Y. Lin, Y. Pan, D. Sun, Y. Liu, Microporous Mesoporous Mater. 311 (2021) 110694.
[43] J. Liu, S. Heidrich, J. Liu, B. Guo, M. Zharnikov, U. Simon, W. Wenzel, C. Wöll, ACS Appl. Nano Mater. 4 (2021) 522–528.
[44] A.E. Burakov, E.V. Galunin, I.V. Burakova, A.E. Kucherova, S. Agarwal, A.G. Tkachev, V.K. Gupta, Ecotoxicol. Environ. Saf. 148 (2018) 702–712.
[45] K. Harsha, P. Senthil, R.C. Panda, J. Mol. Liq. 290 (2019) 111197.
[46] K. Wu, J. Zheng, Y. Huang, D. Luo, Y.Y. Li, W. Lu, D. Li, J. Mater. Chem. C 8 (2020) 16974.
[47] X. Lv, L. Shi, K. Li, B. Li, H. Li, ChemComm 53 (2017) 1860–1863.
[48] H. Fu, Z. Xu, J. Zhang, Chem. Mater. 27 (2015) 205–210.
[49] M. Hoshino, A. Khutia, H. Xing, Y. Inokuma, M. Fujita, IUCrJ 3 (2016) 139–151.

[50] W. de Poel, P. Tinnemans, A.L.L. Duchateau, M. Honing, F.P.J.T. Rutjes, E. Vlieg, R. de Gelder, Chem. – Eur. J. 25 (2019) 14999–15003.
[51] K. ichi Otake, K. Otsubo, T. Komatsu, S. Dekura, J.M. Taylor, R. Ikeda, K. Sugimoto, A. Fujiwara, C.P. Chou, A.W. Sakti, Y. Nishimura, H. Nakai, H. Kitagawa, Nat. Commun. 11 (2020) 1.
[52] B. A, G. Hummer, J. C. Rasaiah and J. P. Noworyta, *Nature*, 2001, 414, 188–190.
[53] Y. Umena, K. Kawakami, J. Shen, N. Kamiya, Nature 473 (2011) 55–59.
[54] H. Sui, B. Han, J.K. Lee, P. Walian, B.K. Jap, Nature 414 (2001) 872–878.
[55] M. A. Rivero-crespo, M. Mon, J. Ferrando-soria, C. W. Lopes, M. Boronat, A. L. Ø, A. Corma, J. C. Hern, L. Miguel, J. J. Calvino, E. V Ramos-fernandez, D. Armentano and E. Pardo, Angew. Chem. Int. Ed., 2018, 57, 17094–17099.
[56] Y. Kubota, M. Takata, R. Matsuda, R. Kitaura, S. Kitagawa, K. Kato, M. Sakata, T. C. Kobayashi, Angew. Chem. Int. Ed. 44 (2005) 920–923.
[57] S. Takamizawa, E.I. Nataka, T. Akatsuka, R. Miyake, Y. Kakizaki, H. Takeuchi, G. Maruta, S. Takeda, J. Am. Chem. Soc. 132 (2010) 3783–3792.
[58] T. Kihara, A. Koide, Adv. Chem. Phys. 33 (1975) 51.
[59] R. Vaidhyanathan, S.S. Iremonger, G.K.H. Shimizu, P.G. Boyd, S. Alavi, T.K. Woo, Science 330 (2010) 650–653.
[60] S.H. Chae, H.C. Kim, Y.S. Lee, S. Huh, S.J. Kim, Y. Kim, S.J. Lee, Cryst. Growth. Des. 15 (2015) 268–277.
[61] M. Guillermo, F. Rey, J. Vito, J. Am. Chem. Soc. 135 (2013) 15986–15989.
[62] P. Liao, D. Zhou, A. Zhu, L. Jiang, R. Lin, J. Zhang, J. Am. Chem. Soc. 134 (2012) 17380–17383.
[63] L. Kloo, H. Svensson, M.J. Taylor, J. Chem. Soc., Dalton Trans. (2000) 1061–1065.
[64] J. Su, S. Yuan, H. Wang, L. Huang, T. Cagin, J. Zuo, H. Zhou, J. Ge, E. Joseph, J. Qin, Nat. Commun. 8 (2008) 1–8.
[65] W. Kosaka, Z. Liu, J. Zhang, Y. Sato, A. Hori, R. Matsuda, S. Kitagawa, H. Miyasaka, Nat. Commun. 9 (2018) 1–9.
[66] J. Zhang, W. Kosaka, Y. Kitagawa, H. Miyasaka, Nat. Chem. 13 (2021) 191–199.
[67] O.T. Qazvini, R. Babarao, S.G. Telfer, Nat. Commun. 12 (2021) 1–8.
[68] J. Su, S. Yuan, T. Wang, C.T. Lollar, J.L. Zuo, J. Zhang, H.C. Zhou, Chem. Sci. 11 (2020) 1918–1925.
[69] F.C. Meldrum, V.J. Wade, D.L. Nimmo, B.R. Heywood, S. Mann, Nature 349 (1991) 684–687.
[70] O. Kasyutich, A. Ilari, A. Fiorillo, D. Tatchev, A. Hoell, P. Ceci, J. Am. Chem. Soc. 132 (2010) 3621–3627.
[71] J.M. Bradley, G.R. Moore, N.E. Le Brun, Curr. Opin. Chem. Biol. 37 (2017) 122–128.
[72] C. Pozzi, S. Ciambellotti, C. Bernacchioni, F. Di Pisa, S. Mangani, P. Turano, Proc. Natl. Acad. Sci. U S A 114 (2017) 2580–2585.
[73] L.L. Yan, L.Y. Yao, V.W.W. Yam, J. Am. Chem. Soc. 142 (2020) 11560–11568.
[74] K. Suzuki, S. Sato, M. Fujita, Nat. Chem. 2 (2010) 25–29.
[75] R. McCaffrey, H. Long, Y. Jin, A. Sanders, W. Park, W. Zhang, J. Am. Chem. Soc. 136 (2014) 1782–1785.
[76] Z. Jiang, Y. Zhao, X. Lu, J. Xie, J. Energy Chem. 55 (2021) 70–79.
[77] J. Coro, L.S.R. Silva, K.I.B. Eguiluz, M. Su, G.R. Salazar-banda, Int. J. Hydrogen Energy 1 (2016) 17944–17959.
[78] J.C. Barnes, E.J. Dale, A. Prokofjevs, A. Narayanan, I.C. Gibbs-hall, C.L. Stern, A. A. Sarjeant, Y.Y. Botros, S.I. Stupp, J.F. Stoddart, J. Am. Chem. Soc. 137 (2015) 2392–2399.
[79] L. Bao, C. Pan, Z. Slanina, F. Uhlik, T. Akasaka, X. Lu, Angew. Chem. 128 (2016) 9380–9384.
[80] J.L. Delgado, M.A. Herranz, N. Martin, J. Mater. Chem. 18 (2008) 1417–1426.
[81] Y. Wang, R. Morales-mart, X. Zhang, W. Yang, Y. Wang, A. Rodr, J.M. Poblet, L. Feng, S. Wang, N. Chen, J. Am. Chem. Soc. 139 (2017) 5110–55116.
[82] C. Foroutan-nejad, J. Vı, R. Marek, M. Patzschke, M. Straka, Phys. Chem. Chem. Phys. 17 (2015) 24182–24192.
[83] X. Zhang, W. Li, L. Feng, X. Chen, A. Hansen, S. Grimme, S. Fortier, D. Sergentu, T.J. Duignan, J. Autschbach, S. Wang, Y. Wang, G. Velkos, A.A. Popov, N. Aghdassi, S. Duhm, X. Li, J. Li, L. Echegoyen, W.H.E. Schwarz, N. Chen, Nat. Commun. 9 (2018) 1–8.
[84] S. Fortier, J.R. Walensky, G. Wu, T.W. Hayton, J. Am. Chem. Soc. 133 (2011) 6894–6897.
[85] R.E. Cramer, R.B. Maynard, J.C. Paw, J.W. Gilje, J. Am. Chem. Soc. 103 (1981) 3589–3590.
[86] J. Zhuang, L. Abella, D.C. Sergentu, Y.R. Yao, M. Jin, W. Yang, X. Zhang, X. Li, D. Zhang, Y. Zhao, X. Li, S. Wang, L. Echegoyen, J. Autschbach, N. Chen, J. Am. Chem. Soc. 141 (2019) 20249–20260.
[87] B. Dong, Y. Yu, Z. Slanina, F. Wang, Y. Lian, F. Uhlik, L. Feng, Inorg. Chem. 61 (2022) 605–612.
[88] A.J. Scott, J. Vallejo, A. Sarkar, L. Smythe, E. Regincós Martí, G.S. Nichol, W.T. Klooster, S.J. Coles, M. Murrie, G. Rajaraman, S. Piligkos, P.J. Lusby, E.K. Brechin, Chem. Sci. 12 (2021) 5134–5142.
[89] B.M. Cossairt, N.A. Piro, C.C. Cummins, Chem. Rev. 110 (2010) 4164–4177.
[90] C. Schwarzmaier, A. Schindler, C. Heindl, S. Scheuermayer, E.V. Peresypkina, A.V. Virovets, M. Neumeier, R. Gschwind, M. Scheer, Angew. Chem., Int. Ed. 52 (2013) 10896–10899.
[91] D. Yang, J. Zhao, L. Yu, X. Lin, W. Zhang, H. Ma, A. Gogoll, Z. Zhang, Y. Wang, X. Yang, B. Wu, J. Am. Chem. Soc. 139 (2017) 5946–5951.
[92] P. Mal, B. Breiner, K. Rissanen, J.R. Nitschke, Science 324 (2009) 1697–1700.
[93] F.J. Rizzuto, D.M. Wood, T.K. Ronson, J.R. Nitschke, J. Am. Chem. Soc. 139 (2017) 11008–11011.
[94] M. Maiss, C.A.M. Brenninkmeijer, Environ. Sci. Technol. 32 (1998) 3077–3086.
[95] M. Rabie, C.M. Franck, Environ. Sci. Technol. 52 (2018) 369–380.
[96] I.A. Riddell, M.M.J. Smulders, J.K. Clegg, J.R. Nitschke, Chem. Commun. 47 (2011) 457–459.
[97] S. Mecozzi, J. Rebek, Chem. – Eur. J. 4 (1998) 1016–1022.
[98] A. Jimenez, R.A. Bilbeisi, T.K. Ronson, S. Zarra, C. Woodhead, J.R. Nitschke, Angew. Chem. 126 (2014) 4644–4648.
[99] M. Alwaeli, V. Mannheim, Energies (Basel) 15 (2022) 4275.
[100] A. Saiz-Lopez, J.M.C. Plane, A.R. Baker, L.J. Carpenter, R. von Glasow, J.C. Gómez Martín, G. McFiggans, R.W. Saunders, Chem. Rev. 112 (2012) 1773–1804.
[101] K.S. Subrahmanyam, D. Sarma, C.D. Malliakas, K. Polychronopoulou, B.J. Riley, D.A. Pierce, J. Chun, M.G. Kanatzidis, Chem. Mater. 27 (2015) 2619–2626.
[102] D. Luo, Y. He, J. Tian, J.L. Sessler, X. Chi, J. Am. Chem. Soc. 144 (2022) 113–117.
[103] M. Pan, K. Wu, J.H. Zhang, C.Y. Su, Coord. Chem. Rev. 378 (2019) 333–349.
[104] J. Jiao, J. Dong, Y. Li, Y. Cui, Angew. Chem., Int. Ed. 60 (2021) 16568–16575.
[105] L.E. MacKenzie, R. Pal, Nat. Rev. Chem. 5 (2021) 109–124.
[106] S.J. Hu, X.Q. Guo, L.P. Zhou, D.N. Yan, P.M. Cheng, L.X. Cai, X.Z. Li, Q.F. Sun, J. Am. Chem. Soc. 144 (2022) 4244–4253.
[107] A. Bavykina, A. Cadiau, J. Gascon, Coord. Chem. Rev. 386 (2019) 85–95.
[108] B.W. Smith, M. Monthioux, D.E. Luzzi, Nature 396 (1998) 323–324.
[109] F.C. Meldrum, C. O'Shaughnessy, Adv. Mater. 32 (2020) 2001068.
[110] J.M. Ha, B.D. Hamilton, M.A. Hillmyer, M.D. Ward, Cryst. Growth Des. 12 (2012) 4494–4504.
[111] Q. Jiang, C. Hu, M.D. Ward, J. Am. Chem. Soc. 135 (2013) 2144–2147.
[112] J. Desarnaud, D. Bonn, N. Shahidzadeh, Sci. Rep. 6 (2016) 23–26.
[113] D. Fu, Y. Su, X. Gao, Y. Liu, D. Wang, J. Phys. Chem. B 117 (2013) 6323–6329.
[114] Y. Liu, Y. Wu, J. Yao, J. Yin, J. Lu, J. Mao, M. Yao, F. Luo, ACS Omega 6 (2021) 18235–18247.
[115] E.L. Smith, A.P. Abbott, K.S. Ryder, Chem. Rev. 114 (2014) 11060–11082.
[116] X. Lan, X. Wang, W. Du, T. Mu, X.Z. Lan, Phys. Chem. Chem. Phys. 23 (2021) 13785–13788.
[117] J.W. Pridgeon, R.M. Pereira, J.J. Becnel, S.A. Allan, G.G. Clark, K.J. Linthicum, J. Med. Entomol. 45 (2008) 82–87.
[118] X. Zhu, C.T. Hu, B. Erriah, L. Vogt-Maranto, J. Yang, Y. Yang, M. Qiu, N. Fellah, M.E. Tuckerman, M.D. Ward, B. Kahr, J. Am. Chem. Soc. 143 (2021) 17144–17152.
[119] J.F. McConnell, Cryst. Struct. Commun. 2 (1973) 459–461.
[120] H. Krishna Murthy, T. Bhat, M. Vijayan, Acta Crystallogr. Sect. B: Struct. Crystallogr. Cryst. Chem. 38 (1982) 315–317.
[121] V. Lopez-Mejias, J.W. Kampf, A.J. Matzger, J. Am. Chem. Soc. 134 (2012) 9872–9875.
[122] K. Zhang, N. Fellah, V. López-Mejías, M.D. Ward, Cryst. Growth Des. 20 (2020) 7098–7103.
[123] C.E. Nicholson, C. Chen, B. Mendis, S.J. Cooper, Cryst. Growth Des. 11 (2011) 1–4.
[124] J. Liu, C.E. Nicholson, S.J. Cooper, Langmuir 23 (2007) 7286–7292.
[125] Q. Liu, J. Wang, H. Wu, S. Zong, X. Huang, T. Wang, H. Hao, Ind. Eng. Chem. Res. 59 (2020) 13024–13032.
[126] K. Allen, R.J. Davey, E. Ferrari, C. Towler, G.J. Tiddy, M.O. Jones, R.G. Pritchard, Cryst. Growth Des. 2 (2002) 523–527.
[127] A.K. Tiwary, Drug Dev. Ind. Pharm. 27 (2001) 699–709.
[128] J. Wang, W. Cao, L. Zhu, J. Wang, R. Lakerveld, Chem. Eng Sci. 226 (2020) 115861.
[129] Y. Kawabata, K. Wada, M. Nakatani, S. Yamada, S. Onoue, Int. J. Pharm. 420 (2011) 1–10.
[130] G. Ward, P.M. Martin-Soladana, P. Martin, R. Tona, N. Garg, N. Douillet, D. Lai, Lab Chip 20 (2020) 1815–1826.
[131] S.R. Wilson-Whitford, R.W. Jaggers, B.W. Longbottom, M.K. Donald, G.J. Clarkson, S.A.F. Bon, ACS Appl. Mater. Interfaces 13 (2021) 5887–5894.